

# Clustering of Luminous Red Galaxies IV: Baryon Acoustic Peak in the Line-of-Sight Direction and a Direct Measurement of $H(z)$

Enrique Gaztañaga<sup>1</sup>, Anna Cabré<sup>1</sup> & Lam Hui<sup>2</sup>

<sup>1</sup>*Institut de Ciències de l'Espai, IEEC-CSIC, F. de Ciències, Torre C5 par-2, Barcelona 08193, Spain*

<sup>2</sup>*Institute for Strings, Cosmology and Particle Physics, Columbia Astrophysics Laboratory, and Department of Physics, Columbia University, New York, NY 10027, U. S. A.*

30 October 2018

## ABSTRACT

We study the clustering of LRG galaxies in the latest spectroscopic SDSS data releases, DR6 and DR7, which sample over  $1 \text{ Gpc}^3/h^3$  to  $z=0.47$ . The 2-point correlation function  $\xi(\sigma, \pi)$  is estimated as a function of perpendicular  $\sigma$  and line-of-sight  $\pi$  (radial) directions. We find a significant detection of a peak at  $r \simeq 110\text{Mpc}/h$ , which shows as a circular ring in the  $\sigma - \pi$  plane. There is also significant evidence for a peak along the radial direction whose shape is consistent with its originating from the recombination-epoch baryon acoustic oscillations (BAO). A  $\xi(\sigma, \pi)$  model with no radial BAO peak is disfavored at  $3.2\sigma$ , whereas a model with no magnification bias is disfavored at  $2\sigma$ . The radial data enable, for the first time, a direct measurement of the Hubble parameter  $H(z)$  as a function of redshift. This is independent from earlier BAO measurements which used the spherically averaged (monopole) correlation to constrain an integral of  $H(z)$ . Using the BAO peak position as a standard ruler in the radial direction, we find:  $H(z = 0.24) = 79.69 \pm 2.32(\pm 1.29) \text{ km/s/Mpc}$  for  $z=0.15-0.30$  and  $H(z = 0.43) = 86.45 \pm 3.27(\pm 1.69) \text{ km/s/Mpc}$  for  $z = 0.40 - 0.47$ . The first error is a model independent statistical estimation and the second accounts for systematics both in the measurements and in the model. For the full sample,  $z = 0.15 - 0.47$ , we find  $H(z = 0.34) = 83.80 \pm 2.96(\pm 1.59) \text{ km/s/Mpc}$ .

## 1 INTRODUCTION

Luminous red galaxies (LRG's) are selected by color and magnitude to obtain intrinsically red galaxies in SDSS (Eisenstein et al 2001). These galaxies trace a big volume, around  $1 \text{ Gpc}^3 h^{-3}$ , which makes them ideal for studying clustering on large scales (see Hogg et al. 2005). Attention has been paid especially to the baryon acoustic peak around a scale of  $100 \text{ Mpc}/h$ , because of its value as a standard ruler. In Eisenstein et al (2005) the baryon acoustic peak was detected in the spherically averaged two-point correlation function (i.e. the monopole) using LRG's from an earlier SDSS release (about half the size of the final data). Both 2dFGRS and SDSS spectroscopic redshift surveys have been used to constrain cosmological parameters via the galaxy power spectrum (Eisenstein et al. 2004; Sánchez et al. 2006), including information from the baryon acoustic feature (Hütsi 2006a,b; Percival et al. 2007; Sanchez et al. 2009). Photometric LRG catalogs cover a larger volume and larger densities and have also been used to obtain cosmological constraints (Padmanabhan et al. 2007; Blake et al. 2007).

In this paper, as in Papers I (Cabré & Gaztañaga 2009a) and II (Cabré & Gaztañaga 2009b) of this series, we

focus on the LRG's anisotropic redshift space correlation function  $\xi(\sigma, \pi)$ , where  $\pi$  is the line-of-sight (LOS) or radial separation and  $\sigma$  is the transverse separation. There are three sources of anisotropy at scales larger than  $40\text{Mpc}/h$ . It is well known that peculiar motion distorts the correlation function anisotropically (Kaiser 1987). It is also well known that assuming the wrong background cosmology will lead to an anisotropic  $\xi$  (Alcock & Paczynski 1979). What is under-appreciated is that gravitational lensing also introduces an anisotropy of its own to the galaxy correlation function (Matsubara 2000b; Hui et al. 2007, 2008). In this paper, we will present evidence of this lensing distortion in the LOS direction.

A distinct focus of this paper in the series is on the baryon acoustic oscillation (BAO) feature in  $\sigma - \pi$  plane. In principle, it can be used as a standard ruler to measure both the Hubble expansion rate  $H(z)$ , via its observed redshift span in the radial direction, and the angular diameter distance  $D_A(z)$ , via its observed angular size in the transverse direction (Blake & Glazebrook 2003; Seo & Eisenstein 2005). We will implement this idea to measure  $H(z)$ . We are aided in this endeavor by two effects. Redshift distortions

in the LOS direction make the  $\xi$  negative on intermediate scales ( $\sim 50 - 90$  Mpc/h), while magnification bias gives  $\xi$  a positive boost especially on large scales ( $\gtrsim 100$  Mpc/h). This combination enhanced the contrast of the radial BAO peak with respect to the BAO in the perpendicular direction. Because the noise is shot-noise dominated any increase in the signal, such as bias or magnification bias, increase the signal-to-noise and helps the BAO detection. We will show that the shape of the correlation function in the radial direction is in good agreement with the predictions. We will also validate the interpretation of the feature as baryon acoustic in nature by studying its appearance in directions away from the radial direction, and performing a parametric fit to the monopole.

It is useful to point out some related earlier work. Redshift distortions in the LRG's and quasars at  $z \sim 0.55$  have been studied using the 2dF-SDSS LRG and QSO Survey (2SLAQ Cannon & etal 2007; Ross et al. 2007; da Ángela et al. 2008; Wake et al. 2008). Okumura et al. (2008) measured  $\xi(\sigma, \pi)$  away from the LOS direction in the SDSS using a sample similar to ours: they used about 47000 LRG's over a redshift range of 0.16 – 0.47 while we use 75000 LRG's over  $z$  of 0.15 – 0.47. None of the earlier papers attempted a direct measurement of  $H(z)$  from the baryon feature in the LOS direction.

This paper is organized as follows. Section 2 gives a summary of the theory, including a brief introduction to magnification bias. In section 3 we perform an analysis of the clustering signal around the position of the BAO peak, both in the monopole and in the  $\sigma - \pi$  plane, especially in the radial direction, from which we obtain the Hubble parameter  $H(z)$  in section 4. We end with a conclusion in section 5, where we deduce implications for the dark energy equation of state, and where we emphasize the need for further theoretical work on the nonlinear coupling between peculiar motion and magnification bias.

## 2 THEORY

The 2-point correlation function,  $\xi(\vec{r})$ , is defined by the joint probability that two galaxies are found in two volume elements  $dV_1$  and  $dV_2$  placed at separation  $\vec{r}$  (see Peebles 1980):

$$dP_{12} = n^2[1 + \xi(r)]dV_1dV_2 \quad (1)$$

where  $n$  is the mean number density of galaxies.

We can split the distance  $\vec{r}$  into its component along the line-of-sight (LOS)  $\pi$  and perpendicular to the LOS  $\sigma$ , where  $r^2 = \pi^2 + \sigma^2$ . Azimuthal symmetry implies  $\xi$  is in general a function of  $\pi$  and  $\sigma$  alone.

The correlation  $\xi(\sigma, \pi)$  is related to the power spectrum by a Fourier transform:

$$\xi(\sigma, \pi) = \int P_s(\vec{k}) e^{-i\vec{k}\vec{r}} \frac{d^3k}{(2\pi)^3} \quad (2)$$

Note that the use of  $\pi$  to denote the LOS separation is conventional. Hopefully the reader will not confuse it with the numerical constant  $\pi$  as in  $(2\pi)^3$ .

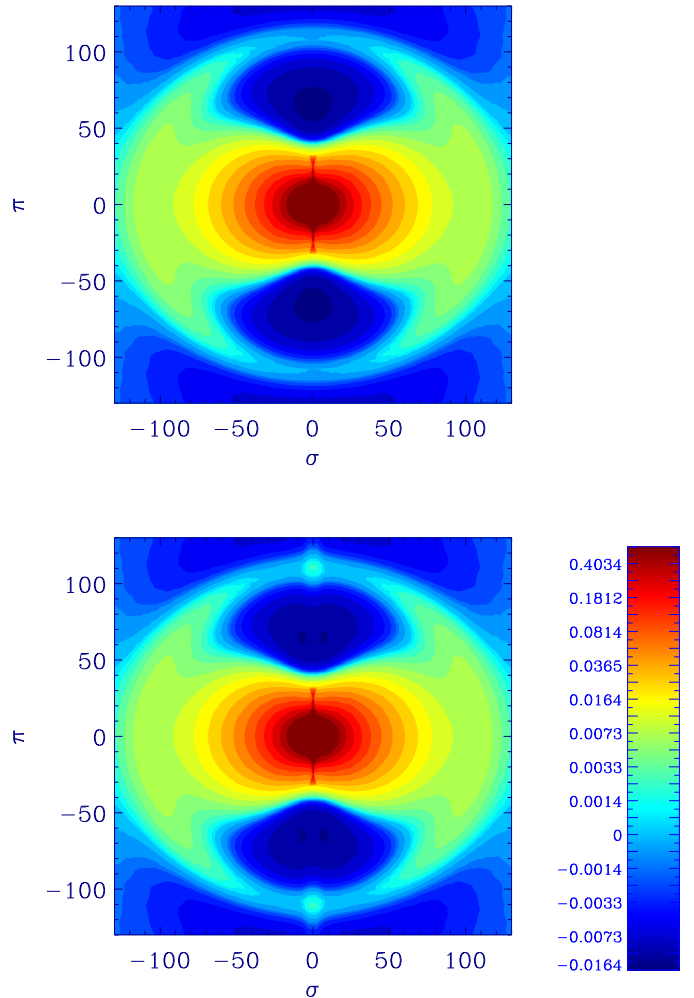


**Figure 1.** *Top panel:* Theoretical  $\xi(\sigma, \pi)$  with linear redshift space distortions convolved with a dispersion model, assuming a cosmology and bias (linear and non-linear) as observed in LRG in paper I and II. Note the ring around  $\simeq 100$  Mpc/h that becomes narrow and less prominent in the radial direction. *Bottom panel:* same with magnification bias added (slope = 2 to see clearly the effect). The main effect is the boosting of the BAO peak in the  $\pi$  direction. In both cases we take into account the bin smoothing at 5Mpc/h.

### 2.1 Redshift Distortions by Peculiar Motion

In the large-scale linear regime, and in the plane-parallel approximation (where galaxies are taken to be sufficiently far away from the observer that the displacements induced by peculiar velocities are effectively parallel), the distortion caused by coherent infall velocities takes a particularly simple form in Fourier space (Kaiser 1987):

$$P_s(\vec{k}) = (1 + \beta\mu_k^2)^2 P_{gg}(k). \quad (3)$$

where  $P_{gg}(k)$  is the power spectrum of galaxy density fluctuation  $\delta_g$ ,  $\mu$  is the cosine of the angle between  $\vec{k}$  and the

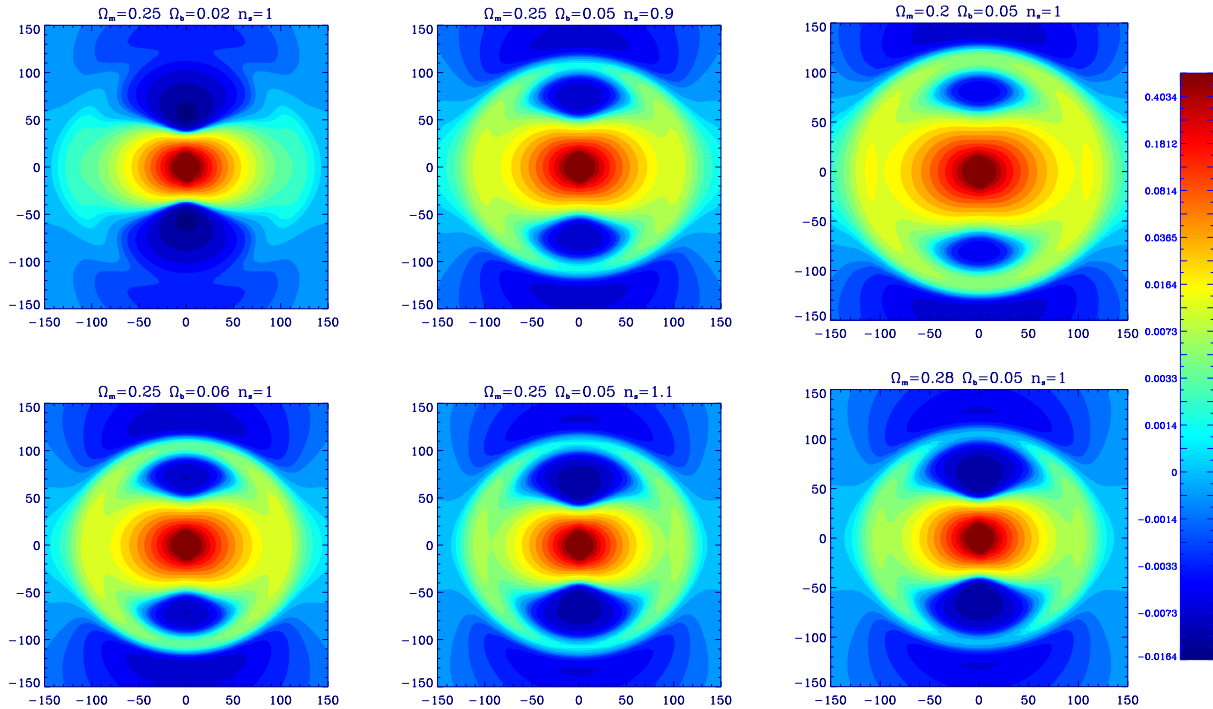


**Figure 2.** Same as Fig.1, with different panels corresponding to different cosmological parameters as labeled in the figures: left panels show change with the baryon density  $\Omega_b$ , middle panels with the scalar spectral index  $n_s$  and right panels with the matter density  $\Omega_m$ .

line-of-sight, the subscript  $s$  indicates redshift space, and  $\beta$  is the growth rate of growing modes in linear theory, the dimensionless quantity which solves the linearized continuity equation  $\vec{\nabla} \cdot \vec{v} + (a'/a)\beta\delta_g = 0$ , where the prime denotes derivative with respect to conformal time. Assuming that the galaxy over-density  $\delta$  is linearly biased by a factor  $b$  relative to the underlying matter density  $\delta_m$ , i.e.  $\delta_g = b\delta_m$ , and that the velocities are unbiased, the value of  $\beta$  can be approximated by

$$\beta \approx \frac{\Omega_m^{0.55}}{b} \quad (4)$$

(see Hamilton 1992, for a review). After integration in Eq.2, these linear distortions in  $P_s(\vec{k})$  produce a distinctively anisotropic  $\xi(\sigma, \pi)$ . Redshift distortions in the linear regime produce a lower amplitude and sharper baryon acoustic peak in the LOS than in the perpendicular direction because of the coherent infall into large scale overdensities. This is illustrated in top panel of Fig.1. A characteristic feature of this effect is a valley of negative correlations (in blue) on scales between  $\pi = 50 - 90$  Mpc/h, which as we will show is in good agreement with our measurements from real data. Such a valley is absent without redshift distortions.

Redshift space distortions on smaller scales (commonly called the finger-of-god effect) are often approximated by a dispersion model where  $\xi$  is convolved with a distribution of pairwise velocities, parametrized by a single parameter  $\sigma_v$ . Details are presented in Paper II (Cabr e & Gazta naga 2009b). Note that in Fig. 1, as in all  $\xi(\sigma, \pi)$  contour diagrams

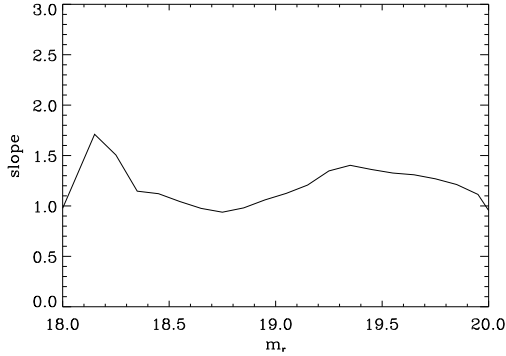
of this paper, bins of  $5 \text{ Mpc/h} \times 5 \text{ Mpc/h}$  are used. The finger-of-god effect is much suppressed by using bins of this size. Readers interested in an analysis that brings out this effect rather than suppressing it are referred to Paper II (Cabr e & Gazta naga 2009b).

Fig.2 shows how the shape of  $\xi(\sigma, \pi)$  changes with cosmological parameters: baryon density  $\Omega_b$ , initial spectra index  $n_s$  and cold dark matter density  $\Omega_m$ . Note how the BAO ring becomes more or less asymmetric and how this is correlated with the valley of negative correlations (in blue).

## 2.2 Magnification bias

Gravitational lensing inevitably modulates the observed spatial distribution of galaxies. To lowest order, there are two effects at work. Imagine a number of galaxies located behind some large mass concentration. Dim galaxies that otherwise would not have been detected are brought into one's sample by the lensing magnification. This increases the observed number density of galaxies. On the other hand, magnification also increases the apparent area, which leads to a drop in the observed number density of galaxies. The net lensing effect, known as magnification bias, is controlled by the slope of the number counts (Turner et al. 1984; Webster et al. 1988; Fugmann 1988; Narayan 1989; Schneider 1989; Broadhurst et al. 1995; Moessner et al. 1998):

$$s = \frac{d \log_{10} N(< m)}{dm} \quad (5)$$



**Figure 3.** LRG number count slope  $s$  as a function of limiting apparent magnitude  $m_r$ , using all SDSS DR6 photometric catalog.

where  $N(< m)$  refers to the number of galaxies in the survey with apparent magnitude brighter than  $m$ . Note that to estimate  $s$  we need to know  $N(< m)$  for magnitudes that are fainter than our spectroscopic limit of  $m = 19.2$ . We can use the parent photometric DR6 sample, which is deeper but does not have redshifts. Fig. 3 shows the estimation for  $s$  in the SDSS LRG DR6 galaxies extracted from the full (parent) photometric catalog. Because the parent catalog is deeper, it also goes further in redshift. Thus a fraction of the fainter galaxies in the photometric catalog will be at different redshift to the galaxies in our spectroscopic redshift samples. Also note that different selection effects go into the photometric and spectroscopic samples. Thus the true number count slope in the spectroscopic sample is somewhat uncertain and might be different for different redshift slices<sup>1</sup>. Our magnitude cut is around 19.2, where  $s$  seems to lie close to 1.5, with a potentially large uncertainty if evolutionary and/or selection effects turn out to be important. Given that variations of  $s$  in Fig.3 are of order  $\Delta s \simeq 0.5$  we consider a range around  $s = 1.0 - 2.0$  for our modeling of magnification bias.

The observed galaxy overdensity  $\delta_{obs}$  is related to the intrinsic (or true) galaxy overdensity  $\delta_g$  by:

$$s\delta_{obs} = \delta_g + \delta_\mu \quad (6)$$

where  $\delta_\mu = (5s - 2)\kappa$ , with  $\kappa$  being the lensing convergence which is simply a weighted LOS integral of the mass fluctuation  $\delta_m$  (see Hui et al. 2007, for details)

Including linear redshift distortions by peculiar motion is straightforward:

$$\delta_{obs} = \delta_g + \delta_\mu + \delta_v \quad (7)$$

where  $\delta_v = (1 + \bar{z})H(\bar{z})^{-1}\partial v_\pi/\partial\pi$  with  $\bar{z}$  being the mean redshift, and  $v_\pi$  being the peculiar velocity in the  $\pi$  direction. Squaring the above expression, the net observed correlation

function is therefore

$$\xi_{obs} = \xi_{gg} + \xi_{gv} + \xi_{vg} + \xi_{vv} + \xi_{g\mu} + \xi_{\mu g} + \xi_{\mu\mu} \quad (8)$$

The velocity-magnification cross-terms are absent by virtue of Limber approximation and linear theory (see Matsubara 2000b; Hui et al. 2008, for details). The first term is the true or intrinsic galaxy clustering signal. The next three terms account for the Kaiser effect. These four terms together are the real space analog of what is shown in Eq.(3). The rest of the terms account for magnification bias: the magnification-magnification term is very small at our moderate redshifts of interest; we need focus only on the galaxy-magnification cross terms (Hui et al. 2007, 2008). They are capable of altering significantly the observed correlation function on large scales. Taylor expanding in  $\pi/\bar{\chi}$ , where  $\pi = |\chi_1 - \chi_2|$  is the LOS separation between a pair of galaxies and  $\bar{\chi}$  is the mean sample depth, the galaxy-magnification cross correlation can be written as (Hui et al. 2007):

$$\begin{aligned} \xi_{g\mu}(\chi_1, \boldsymbol{\theta}_1; \chi_2, \boldsymbol{\theta}_2) + \xi_{\mu g}(\chi_1, \boldsymbol{\theta}_1; \chi_2, \boldsymbol{\theta}_2) = \\ \frac{3}{2}H_0^2\Omega_m(5s - 2)(1 + \bar{z})|\chi_1 - \chi_2| \\ \int \frac{d^2k_\perp}{(2\pi)^2}P_{gm}(\bar{z}, k_\perp)e^{i\mathbf{k}_\perp \cdot \bar{\chi}(\boldsymbol{\theta}_1 - \boldsymbol{\theta}_2)} \end{aligned} \quad (9)$$

where  $P_{gm}$  is the galaxy-mass power spectrum. Here,  $H_0$  is the Hubble constant today,  $\Omega_m$  is the matter density,  $\bar{z}$  is the mean redshift of the sample in question, and  $\chi$  and  $\boldsymbol{\theta}$  with subscripts label the radial distance and angles of a pair of galaxies.

The above expression shows clearly the anisotropic nature of the lensing corrections to the galaxy correlation function. A large LOS separation  $\pi = |\chi_1 - \chi_2|$  is clearly favored as it should be, since lensing is more effective if the source (background galaxy) and the lens (foreground galaxy) are further apart. On the other hand, a small transverse separation  $\sigma \sim \bar{\chi}|\boldsymbol{\theta}_1 - \boldsymbol{\theta}_2|$  is helpful for boosting the lensing correction. This makes sense because gravitational lensing is strongest when the impact parameter is small. The magnification distortion of the correlation function hence is strongest in the LOS  $\pi$  direction. Note that the intrinsic galaxy clustering strength generally drops with separation, even as the lensing correction increases with the LOS separation  $\pi$ . This means for a sufficiently large LOS separation, the lensing correction could dominate.

It is also important to note that for a small transverse separation  $\sigma$ , the integral of  $P_{gm}$  is dominated by high wavenumbers, including ones where both the mass fluctuations and the galaxy bias are nonlinear. These nonlinear effects can further boost the galaxy-magnification correlation. Indeed, if  $\sigma$  were small enough, one might need to worry about strong lensing effects. But since throughout our analysis, we avoid any pairs with  $\sigma$  less than 0.5 Mpc/h (because of fiber collision issues), we are safely in the weak lensing regime.

The bottom panel of Fig.1 shows the theoretical expectation for  $\xi(\sigma, \pi)$  with magnification bias taken into account. This can be compared against the top panel, which has no magnification bias. There is a clear enhancement of the BAO in the radial direction ( $\sigma = 0$ ). The effect in other directions

<sup>1</sup> Note that the number counts here are limited to some particular redshift range, e.g.  $z=0.15-0.30$ , and should not be confused with the integrated number counts from redshift zero. In other words, the slope of the number count  $s$  here should best be thought of as being related to the slope of the intrinsic luminosity function.

is relatively minor. Here, we have used a small scale galaxy bias similar to that in LRG galaxies (see Fig.4) and a number count slope of  $s = 2$ . The large scale galaxy bias is 2. See §3.8, Jain et al. (2003) and Hui et al. (2007) for further discussions on these numbers.

### 2.3 Beyond Standard Theory

The above discussion of the theory for redshift and magnification distortions is more or less standard (though the anisotropy induced by lensing is not as widely appreciated). There are, however, certain limitations to the standard theory. For instance, the mapping from real to redshift space creates nonlinear effects even on very large scales. A sign of this is that caustics can occur in redshift space even if the real space overdensity is rather modest (Hui et al. 2000). As emphasized by Scoccimarro (2004), depending on the statistics studied, the Kaiser plus dispersion model for redshift distortions can be inaccurate even on linear scales. Similar concerns apply to magnification distortions when peculiar motion are taken into account. The expression in Eq. 8 ignores velocity-magnification cross-correlation. This is justified in linear theory, but not valid once nonlinear effects are taken into account. Moreover, for small values of  $\sigma$  (ie  $\sigma < 5.5$  Mpc/h in our analysis) the lensing effect at large  $\pi$  separations is dominated by the correlation at  $r \simeq \sigma$ , where the clustering is fully non-linear. We need to account for these non-linearities if we want to take the full lensing contribution into account.

We have carried out an investigation of these effects using numerical simulations. The details are described in Appendix A. The main conclusions are: **1.** Eq. (9) seems a good approximation to the true magnification bias correction to the two point function, even after allowing for nonlinear redshift space effects and their coupling with lensing, provided that **2.** the fully nonlinear  $P_{gm}$  is used in the integral in Eq. (9) i.e. nonlinear galaxy bias is important. The second point is crucial and bears repeating. Suppose one is correlating two galaxies that are far apart in the radial direction  $\pi$  but close in the transverse direction  $\sigma$ . One might naively think that since the two galaxies are far apart, only linear galaxy bias needs to be considered. This is not true once the lensing effect is included. A small transverse separation means the lensing impact parameter is small. One is then sensitive to the galaxy-mass correlation on small scales. Recall that the lensing magnification is an integral of mass overdensity along the line of sight. The relevant lensing correction  $\xi_{g\mu}$  comes from correlating the galaxy in the foreground with the lensing magnification of the background. The dominant contribution comes from the portion of the line of sight integral that is in fact close to the foreground galaxy. In other words, a theoretical prediction for  $\xi_{g\mu}$  using a linear galaxy bias (such as by Hui et al. 2007) underestimates the lensing effect for small  $\sigma$ 's, since the true galaxy bias on small scales is expected to rise above the linear value. This is illustrated in Fig. 4, from the analysis in Paper II (Cabr e & Gazta naga 2009b). The net effect on  $\xi_{g\mu}$  is described in Appendix A, Fig. A2.

When modeling data, we can use Eq. (9) with a non-

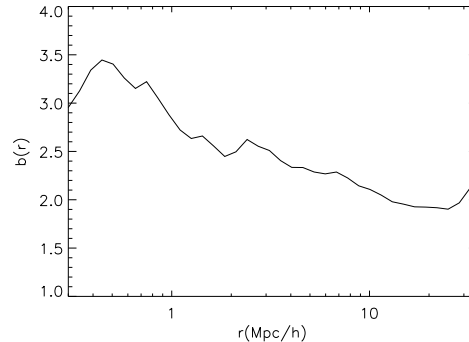


**Figure 4.** This is the observed LRG clustering bias as a function of scale  $r$ , defined by  $b(r) = \sqrt{\xi_{\text{obs}}(r)/\xi_{\text{DM}}(r)}$ , where  $\xi_{\text{obs}}$  is the galaxy correlation function and  $\xi_{\text{DM}}$  is the theoretical nonlinear dark matter correlation, both in real space.

linear galaxy bias taken from Fig. 4. Note that this galaxy bias, while inferred from data, is strictly speaking not the relevant bias to use - what we need is the nonlinear bias relevant for galaxy-mass correlation rather than for galaxy-galaxy correlation. In our modeling in 3.8.2, we will therefore allow an extra overall normalization factor multiplying Eq. (9), which we refer to as  $A$ . We will show that the data favors a non-zero magnification bias correction  $A \neq 0$  at the  $2\sigma$  level, but our estimate for magnification bias  $A = 1$  is 1.5-sigma smaller from the actual best fit for  $A$ . Given the mentioned uncertainties, it is possible the real lensing effect is in fact larger than our prediction.

## 3 ANALYSIS AND RESULTS

### 3.1 Data sample

In this work we use the recent spectroscopic SDSS data releases, DR7 and DR6 (Adelman-McCarthy & etal 2008). We use the same samples and methodology here as presented in Paper I (Cabr e & Gazta naga 2009a) of this series. LRG's are targeted in the photometric catalog, via cuts in the (g-r, r-i, r) color-color-magnitude cube. Note that all colors are measured using model magnitudes, and all quantities are corrected for Galactic extinction following Schlegel et al. (1998). The galaxy model colors are rotated first to a basis that is aligned with the galaxy locus in the (g-r, r-i) plane according to:  $c_{\perp} = (r - i) - (g - r)/4 - 0.18$  and  $c_{\parallel} = 0.7(g - r) + 1.2[(r - i) - 0.18]$ . Because the 4000 Angstrom break moves from the g band to the r band at a redshift  $z \simeq 0.4$ , two separate sets of selection criteria are needed to target LRGs below and above that redshift. The two cuts together result in about 12 LRG targets per  $deg^2$  that are not already in the main galaxy sample. The radial distribution and magnitude-redshift diagrams for these galaxies are shown in Fig.A1 and A12 of Paper I.

We k-correct the r magnitude using the Blanton program 'kcorrect'<sup>2</sup>. We need to k-correct the magnitudes

<sup>2</sup> [http://cosmo.nyu.edu/blanton/kcorrect/kcorrect\\_help.html](http://cosmo.nyu.edu/blanton/kcorrect/kcorrect_help.html)

in order to obtain the absolute LRG magnitudes and eliminate the brightest and dimmest galaxies. We have seen that the previous cuts limit the intrinsic luminosity to a range  $-23.2 < M_r < -21.2$ , and we only eliminate from the catalog a small number of galaxies that lay out of the limits. Once we have eliminated these extreme galaxies, we still do not have a volume limited sample at high redshift. For the 2-point function analysis we account for this using a random catalog with identical selection function but 20 times denser (to avoid shot-noise). The same is done in simulations.

There are about 75,000 LRG galaxies with spectroscopic redshifts in the range  $z = 0.15 - 0.47$  over 13% of the sky. We break the full sample into 3 independent subsamples with similar number of galaxies: low  $z = 0.15 - 0.30$ , middle  $z = 0.30 - 0.40$  and high  $z = 0.40 - 0.47$ . The middle sample has a lower amplitude of clustering because it includes galaxies with a lower luminosity (see Fig.A12 in Paper I). Also note that the radial distribution is quite peaked in the middle sample (see Fig.A1 in Paper I). The resulting clustering in this sample has a low signal-to-noise and we cannot detect the BAO peak in the monopole (see Fig.31 and A13 of Paper I). We will therefore concentrate on results from the full sample, as well as the low and high redshift slices for the BAO detection.

### 3.2 2-point correlation

The two-point correlation function is defined as

$$\xi(\sigma, \pi) = \langle \delta(r_1) \delta(r_2) \rangle \quad (10)$$

where  $\delta(r) = \rho(r)/\bar{\rho} - 1$  is the local density fluctuation about the mean  $\bar{\rho} = \langle \rho \rangle$ , and the expectation value is taken over different realizations of the model or physical process. As mentioned above, the observed correlation function is anisotropic. We estimate the correlation as  $\xi(\sigma, \pi)$ , where  $\pi$  is the separation along the line-of-sight (LOS) and  $\sigma$  is the transverse separation. The absolute separation (in redshift space) is  $r_{12} = \sqrt{\sigma^2 + \pi^2}$ .

In practice, the expectation value above is over different spatial regions in our universe, which are assumed to be a fair sample of possible realizations (see Peebles 1980). A possible complication with this approach is the so-called finite volume effect which leads to an estimation bias, sometimes referred to as the integral constraint bias (e.g. see Hui & Gaztañaga (1999); Bernardeau et al. (2002)). For our samples and scale of interest (ie  $< 150$  Mpc/h) we have checked using a large simulation that such a potential estimation bias is small compared to the errors. We use a simulation about 500 times the volume of the SDSS LRG data (MICEL7680 with  $453 \text{ Gpc}^3/h^3$ ,  $2048^3$  dark matter particles and 107 million halos in a single box; see Fosalba et al. (2008); Crocce et al. (2009)) to estimate the ‘‘true’’ correlation. We then split this large simulation into 216 mocks and estimate the mean and error of the 2 and 3-point correlation functions in the 216 subsamples (each similar to the SDSS LRG samples). We find that the mean agrees well with the true value estimated from the full simulation, well within the error estimated from the dispersion among the subsamples. In other words, any possible estimation bias, on our

scales of interest, is much smaller than the errorbar. The ratio defined by the difference between the true correlation (from the full MICE7680 simulation) and the mean correlation in 216 smaller mocks (cut out of the full MICE7680 simulation) divided by the dispersion (the error) indicates how large is the integral constrain bias as compare to the error. It turns out to be insignificant, always smaller than 0.05% of the error in both dark matter and halo mocks. For the monopole we also find that the integral constraint bias is always smaller than 0.1% of the error for all the scales in our analysis, ie  $s < 150$  Mpc/h (see also paper I and III where we show several examples of this).

### 3.3 Estimation of $\xi(\sigma, \pi)$ and diagonal errors

To estimate the correlation  $\xi(\sigma, \pi)$ , we use the estimator of Landy & Szalay (1993),

$$\xi(\sigma, \pi) = \frac{DD - 2DR + RR}{RR} \quad (11)$$

with a random catalog  $N_R = 20$  times denser than the SDSS catalog. We find similar results when we use other similar estimators, such as  $DD/RR - 1$  and  $DD/DR - 1$  or estimators based on pixel density fluctuations (ie Barriga & Gaztañaga (2002)). The random catalog has the same redshift (radial) distribution as the data, but smoothed with a bin  $dz = 0.01$  to avoid possible cancellation of intrinsic correlations in the data. The random catalog also has the same mask. (We will test robustness against variations in the choice of mask and the radial selection function below.) We count the pairs in bins of separation along the line-of-sight (LOS),  $\pi$ , and across the sky,  $\sigma$ . The LOS distance  $\pi$  is just the difference between the radial comoving distances in the pair. The transverse distance  $\sigma$  is given by  $\sqrt{s^2 - \pi^2}$ , where  $s$  is the net distance between the pair. We use the small-angle approximation, as if we had the catalog at an infinite distance, which is accurate until the angle that separates the galaxy pair in the sky is larger than about 10 degrees for  $\xi(\sigma, \pi)$  (see Szapudi (2004) and Matsubara (2000a)). This condition corresponds to transverse scales larger than  $\sigma = 80$  Mpc/h ( $\sigma = 165$  Mpc/h) for galaxies at  $z=0.15$  ( $z=0.34$ ).

There are two sources of error or variance in the estimation of the two-point correlation: a) *shot-noise variance* which is inversely proportional to the number of pairs in each separation bin b) *sampling variance* which scales with the amplitude squared of the correlation. It is easy to check that for the size and number density of our sample, the shot-noise term dominates over the sampling variance error. DM particles have a much higher density than LRG galaxies and for them shot-noise is negligible. We can then dilute the DM particles to check how and when shot-noise dominates over sampling variance. We confirm this using the same simulation MICE7680 mentioned above. We create out of the large box 216 independent mock catalogs with same density than the observed LRG galaxies. Fig. 5 shows the error (square root of the variance) of the line-of-sight  $\xi$  for dark matter (black solid line) and halos (red solid line), computed from the dispersion between the 216 mocks - this is by definition the true error. Note that we dilute DM particles to match the observed LRG density (and  $N(z)$  distribution) so now

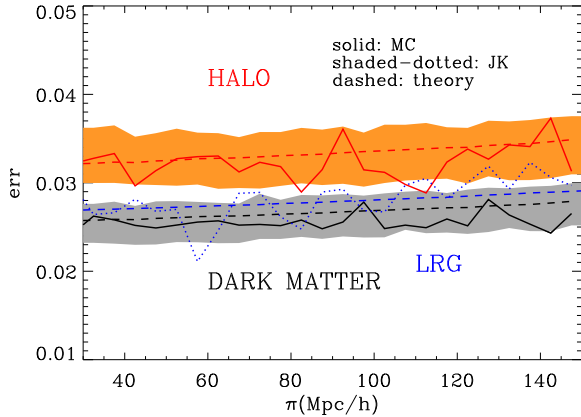


**Figure 5.** In this figure we show different error estimates for the 2-point correlation in the line-of-sight direction  $\pi$ , averaged over  $\sigma = 0 - 5$  Mpc/h. The black solid line and red solid line shows the dispersion for dark matter and halos respectively computed from 216 mock catalogs (the dark matter mocks are at  $z=0.3$ , and the halo mocks are at  $z=0$  chosen with a large scale bias of 1.9). We also calculate the Jack-knife (JK) error for each mock and we plot its dispersion as a shaded region (gray for dark matter and orange for halos). For comparison, we also show the JK error for the real sample of LRGs (blue dotted line). The dashed lines show the error estimates from our analytic model for dark matter (black), halos (red) and LRGs (blue) respectively (see text).

dark matter mocks are also dominated by shot-noise error due to the low density. We compare this error against two approximations: Jack-knife error (Gray and orange shaded regions for dark matter and halos respectively), and an analytic error-estimate (black dashed line and red dashed line for dark matter and halos respectively). The analytic estimate takes the simple form  $\Delta\xi = \alpha_{\text{noise}} \Delta\xi_{\text{Poisson}}$ , where  $\Delta\xi_{\text{Poisson}}$  is simply one over root  $N$  shot noise where  $N$  is the number of pairs at the separation bin of interest. For dark matter mocks,  $\alpha_{\text{noise}} = 1$  works very well, but as discussed in Paper I, the halos or groups do not quite follow a Poisson distribution and their relevant  $\alpha_{\text{noise}} = 1.4$ . The latter is consistent with the findings of others Smith et al. (2007) that massive halos, by virtue of exclusion zones around them, do not have Poissonian shot noise. Fig. 5 shows that both Jack-knife and analytic error estimates work fairly well. For comparison, we also show the Jack-knife error for the LRGs in real data (blue dotted line) and the corresponding analytic estimate (blue dashed line). The agreement between them confirms the validity of our analytic error model, which we will adopt for the rest of this paper. Note that the LRG errors are in-between the DM and halo errors because of the small differences in number density and value of  $\alpha_{\text{noise}}$ .

### 3.4 The covariance matrix

We also use the galaxy (halo) mocks to estimate the covariance matrix between bins in the whole  $\xi(\pi, \sigma)$  plane. Figure 6 shows the covariance for 5 Mpc/h bins in the LOS, normalized to the corresponding variance (ie diagonal elements

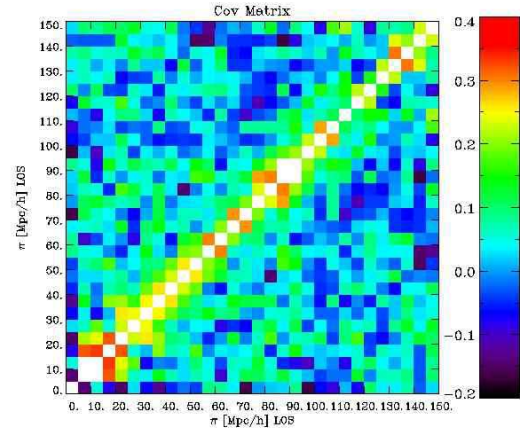


**Figure 6.** Covariance matrix (relative to the variance) for LOS correlation in 5 Mpc/h bins. Even if the covariance is not negligible close to the diagonal, results in our analysis are very similar when we assume a diagonal matrix.

are unity). Full details of this estimation are given in Paper I. The figure shows that at scales  $\pi > 20$  Mpc/h the covariance is quite small. It is smaller than 10% in most of the plane, except in the bins closer to the diagonal where it can be larger but still lower 30%. At the BAO position  $\pi \simeq 110$  Mpc/h the covariance is lower than 10% for all bins. We do our analysis using this covariance matrix, but we have checked that results are very similar when we assume a diagonal matrix (eg see Fig.16), so that in practice the covariance can be neglected.

### 3.5 Results for $\xi(\sigma, \pi)$

In Fig.7 we see the redshift-space correlation function  $\xi(\sigma, \pi)$  for the complete catalog ( $z=0.15-0.47$ ), and for two different slices in redshift:  $z = 0.15 - 0.3$  and  $z = 0.40 - 0.47$ . Recall from the top panel of Fig. 1 that, without magnification bias, the conventional expectation is that one should see a less prominent BAO peak in the LOS direction  $\pi$  than in other directions. Instead, we see from the data, Fig. 7, that the observed BAO peak actually gets more pronounced along the LOS direction, in qualitative agreement with the bottom panel of Fig. 1 which includes magnification bias. Indeed, we see a very nice ring associated with the BAO peak in the data. Note also in the data, we see these valleys of negative correlations (blue) on scales of  $\pi = 50 - 90$  Mpc/h, which are in accord with the predictions of Kaiser distortions (Fig. 1).

In separating  $\sigma$  from  $\pi$  in the data we have assumed the plane-parallel approximation. This introduces a distortion of the BAO scale in the perpendicular direction  $\sigma > 100$  Mpc/h when  $\pi$  is small. This can be clearly seen in the plots, where there is an artificial concentration of the signal at an angle of a few tens of degrees away from the  $\pi = 0$  axis, which produces an X shape in our  $\sigma - \pi$  diagrams, especially at large  $\sigma$ 's. In reality, this signal originates from smaller angles. This effect is explicitly demonstrated in our simulations (see Fig.A14 of Paper I Cabré & Gaztañaga 2009a). In the

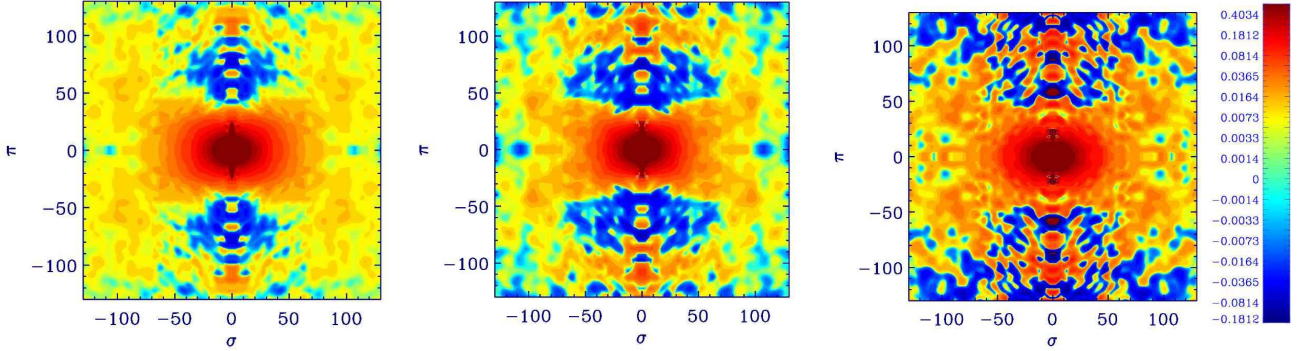


**Figure 7.** Measurements of  $\xi(\pi, \sigma)$  from different redshift slices. From left to right:  $z=0.15-0.47$  (all),  $z=0.15-0.30$  and  $z=0.40-0.47$ .

Appendix of Paper I we show how to correct for this effect by removing some of the pairs in the calculation. This is not the best possible approach, since it throws away information, but it shows the origin of this strange X shape feature at large  $\sigma$ 's. (Matsubara 2000a, see also Fig.9 in). Note, however, that neither the LOS clustering ( $\sigma = 0$ ) nor the monopole, studied here, are affected by this artificial distortion.

We use a fiducial flat model with matter density  $\Omega_m = 0.25$  and Hubble constant  $h = 0.72$  to convert the observed redshifts and angles into distances. Unless stated otherwise we also assume baryon density  $\Omega_b = 0.045$ , and spectral index  $n_s = 0.98$  as the concordance  $\Lambda$ CDM model ( $w = -1$  for the dark energy equation of state).

### 3.6 The Monopole

As a first step in studying the BAO, we look at the monopole, which is the average of  $\xi(\sigma, \pi)$  over orientations:

$$\xi_0(r) = \int_{-1}^1 \xi(\sigma, \pi) \frac{d\mu}{2} \quad (12)$$

where  $r = \sqrt{\sigma^2 + \pi^2}$  and  $\mu = \pi/r$ . Fig. 8 shows the observed monopole (solid line with gray area denoting errorbar) in different redshift slices. The BAO peak is clearly visible. One way to verify its significance is to perform a parametric fit and see if a non-zero baryon density  $\Omega_b$  is required by data. We use 4 parameters:  $\Omega_m h^2$ ,  $\Omega_b h^2$ ,  $n_s$  and an overall amplitude  $Amp$ . Our model is essentially linear theory, but includes non-linear effects according to re-normalized perturbation theory (RPT) at the BAO peak, as described in Crocce & Scoccimarro (2008). Magnification bias is negligible for the monopole. As is demonstrated in Fig. 10 of Paper I, the ratio of the monopole to the real space correlation function is constant on scales larger than about 10 Mpc/h, consistent with the Kaiser model. This is why we fit the data with a single amplitude  $Amp$  which is supposed to account for  $\sigma_8$ , galaxy bias and the redshift distortion boost, all rolled into one. To be conservative, only data on scales larger than 20 Mpc/h are used in our fit. Covariance between different scales is taken into account, using the error model developed and tested in Paper I. Magnification bias

is not included in our fits because its effect on the monopole is quite small at our moderate redshifts (Hui et al. (2007)).

The resulting constraints are shown in Fig. 9, and the corresponding best-fit monopole is shown as a dashed line in Fig. 8. The  $\chi^2$  values quoted in the caption are obtained by applying singular value decomposition to the covariance matrix, keeping modes with the smallest 7 eigenvalues, though the fits are robust against varying this number.

In order to calculate the covariance, we have taken 216 mock catalogs with the same characteristics than LRG galaxies. Moreover, we can calculate the JK covariance for each mock and compute the mean value over all the mock catalogs. This covariance is very similar to the Monte Carlo one but smoother so we use the JK one to calculate  $\chi^2$ . This is extensively explained in Appendix A3 of Paper I.

There is some tension between our best fit  $\Omega_b$  (or  $\Omega_b h^2$ ) and the WMAP5 value Komatsu et al. (2008) for the same model (flat universe with  $w=-1$ ). Our best fit values tend to be higher. A higher  $\Omega_b$  leads to a more prominent BAO peak, as illustrated in Fig. 10. However, it should be emphasized that in the low redshift slice  $z = 0.15 - 0.30$  and in the full sample  $z = 0.15 - 0.47$  the best fit  $\Omega_b h^2$  is less than 2-sigma away from the standard WMAP5 value of 0.22, though the discrepancy is larger in the high redshift slice  $z = 0.40 - 0.47$ . It is also worth noting that there is more room for accommodation once more parameters are allowed to vary, such as the dark energy equation of state  $w$  and the neutrino mass. A more detailed analysis of this is presented in Sanchez et al. (2009).

### 3.7 The BAO Ring

Recall from Eq. 12 that the monopole receives most of its weights from orientations close to the transverse direction (i.e. the measure  $d\mu$  equals  $\sin\theta d\theta$ , where  $\theta$  is the angle with respect to the radial direction). Let us therefore consider briefly the reality of the BAO peak in other directions, including those close to the LOS or radial direction. In Fig. 11, we show the signal-to-noise of  $\xi$  in the  $\sigma - \pi$  plane for the redshift slice  $z = 0.15 - 0.3$ . This complements the  $\xi(\sigma, \pi)$  signal plot in the middle panel of Fig. 10. The signal-to-noise shown in Fig. 11 is for each pixel of size 5 Mpc/h by 5 Mpc/h (the same pixel size is used throughout this paper



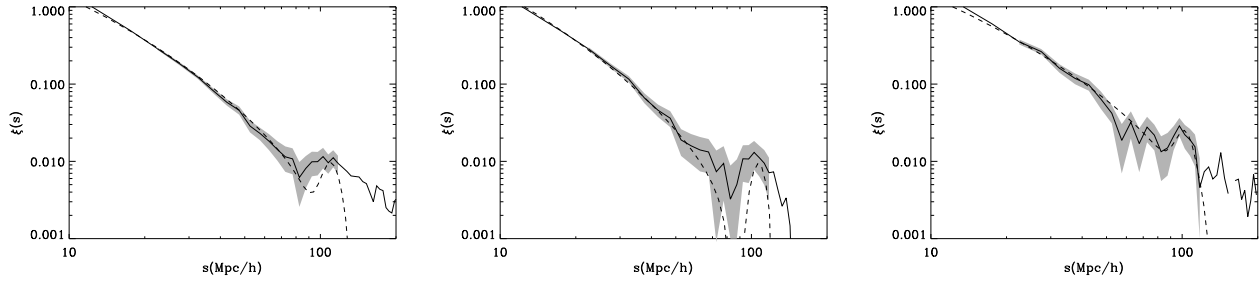


**Figure 8.** Measured monopole with errors (solid line with gray area) compared with the best fit model (dashed line), which uses the scales 20 – 120 Mpc/h (20 log bins). *Left panel:* corresponds to the full sample ( $z=0.15-0.47$ ), where we find  $\chi^2 = 3.4$  (best fit is  $\Omega_m h^2 = 0.12$ ,  $\Omega_b h^2 = 0.026$ ). *Middle panel:* corresponds to the slice  $z=0.15-0.30$ , where we find  $\chi^2 = 1.9$  (best fit is  $\Omega_m h^2 = 0.132$ ,  $\Omega_b h^2 = 0.028$ ). *Right panel:* corresponds to the slice  $z=0.40-0.47$  with  $\chi^2 = 4.8$  (best fit is  $\Omega_m h^2 = 0.124$ ,  $\Omega_b h^2 = 0.04$ ). Allowed values are shown in Fig.9.

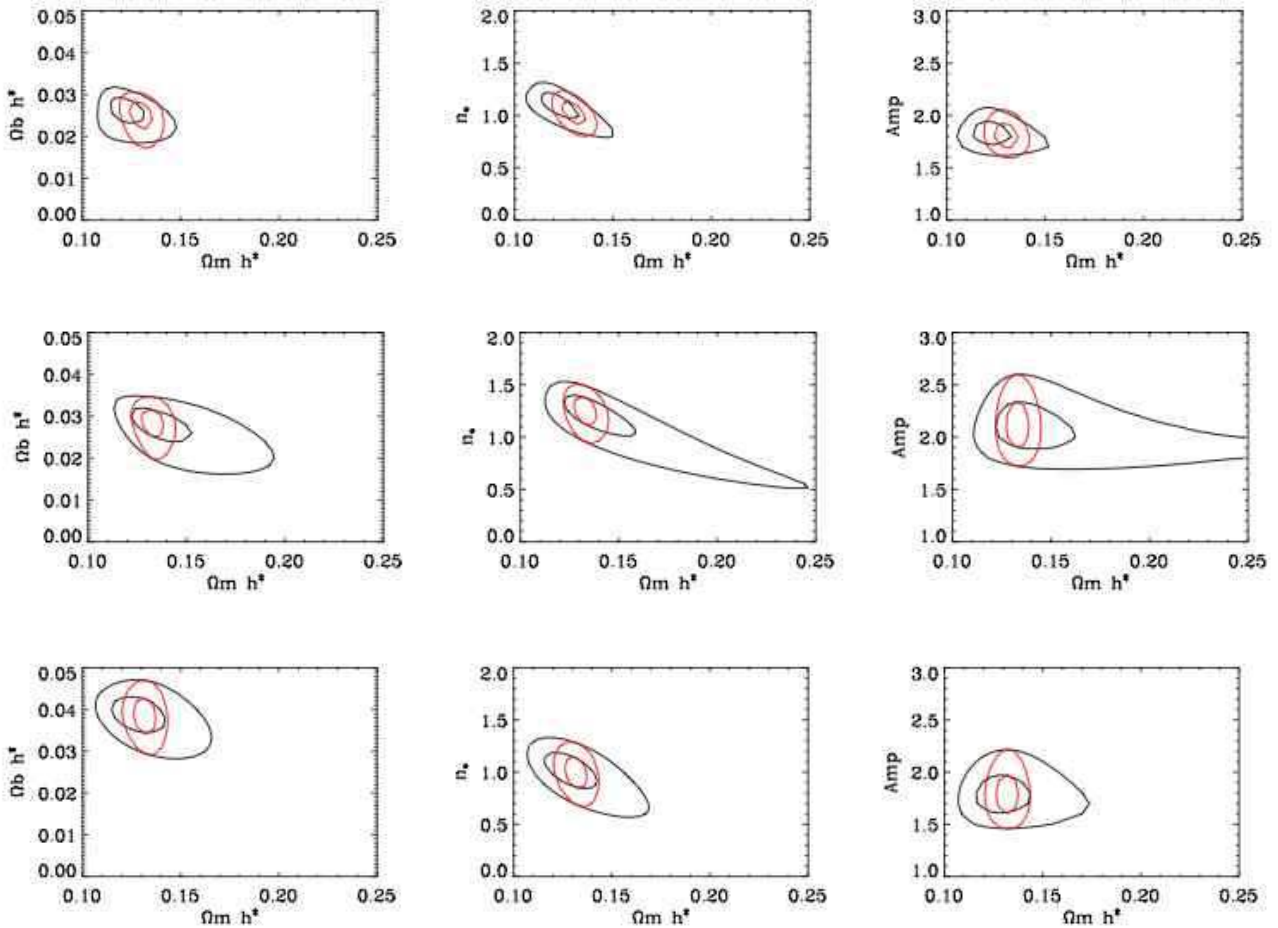


**Figure 9.** Best fit contours (1 and 2-sigma with 1dof) for cosmological parameters in a fit to the monopole. Top, middle and bottom panels correspond to redshift slices  $z=0.15-0.47$ ,  $z=0.15-0.30$  and  $z=0.40-0.47$  respectively. The smaller inner (red) contours use a prior of  $\Omega_m h^2 = 0.1326 \pm 0.0063$  from WMAP5.

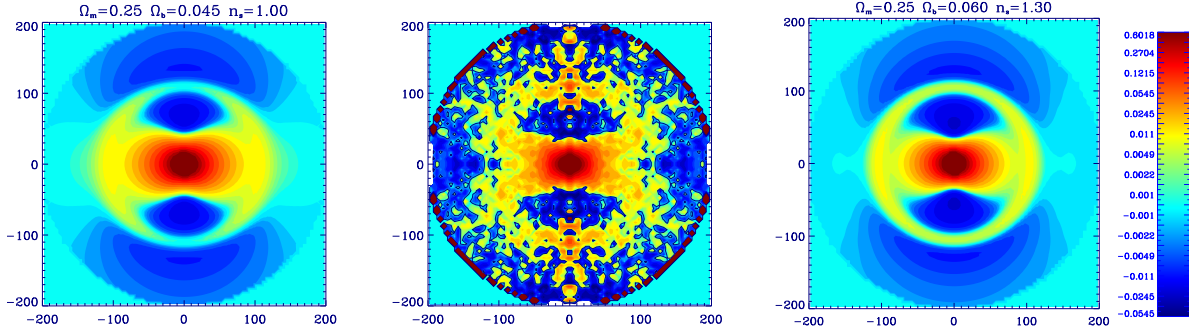


**Figure 10.** A comparison of  $\xi(\sigma, \pi)$  in data and models for the  $z=0.15-0.30$  slice. Left panel corresponds to a standard cosmology (low  $\Omega_b = 0.045$  and  $n_s = 1.0$ ) model, while the right panel has a more prominent BAO peak ( $\Omega_b = 0.06$  and  $n_s = 1.3$ ), which corresponds to the best fit monopole model to the same data. Middle panel shows the data using the same color scheme.

in all of our  $\xi(\sigma, \pi)$  plots). Note that there is covariance between pixels, and so this figure should be interpreted with some care (see Paper I). Nonetheless, it demonstrates the high quality detection of a BAO ring in the  $\sigma - \pi$  plane. The triangle highlights the region  $\pi > \sigma$ , which receives not much weight in the monopole, but where the BAO ring still shows up nicely. Note that the  $(S/N)^2$  shown is modulated by the sign of the signal: the (blue) valley of negative correlations at  $\pi \sim 50-90$  Mpc/h - in accord with the predictions of the Kaiser effect - are detected with significance as well. The overall coherent structure of a negative valley before a positive BAO peak (at just the right expected scales) is quite striking, and cannot be easily explained away by noise or systematic effects.

Fig. 11 suggests that there is sufficient information in the data to separately constrain the angular diameter distance  $D_A(z)$  and the Hubble expansion rate  $H(z)$ , as discussed in §1. That is to say, there is in principle the exciting possibility of determining both quantities, beyond measuring the combination  $(D_A^2/H)^{1/3}$  from the monopole as is customarily done (Eisenstein & etal 2005; see also Appendix A of Hui et al. 2008). In this paper, we will focus on the derivation of  $H(z)$  from clustering in the radial direction, in part because, as discussed earlier in §3, the plane parallel approximation that we have adopted introduces artificial distortions to the signal at large  $\sigma$ 's. This does not affect the analysis here which focus on LOS and monopole but will have an impact in  $\xi(\pi, \sigma)$ . Modeling the wide-angle effects is possible, and is something we hope to pursue in the future.

On scales larger than 120 Mpc/h we also find some excess (i.e. away from null) signal but the amplitude is lower and the sign alternates between positive and negative values and is less coherent than the positive or negative regions at smaller scales. This excess signal on larger scales is also found in the monopole for some of the redshift slices. In the Appendix of Paper I we look for possible systematic effects that could produce this excess. By changing the mask in extreme ways, it is possible to reduce the amplitude of these excess fluctuations on very large scales (see Fig.A8 in Paper

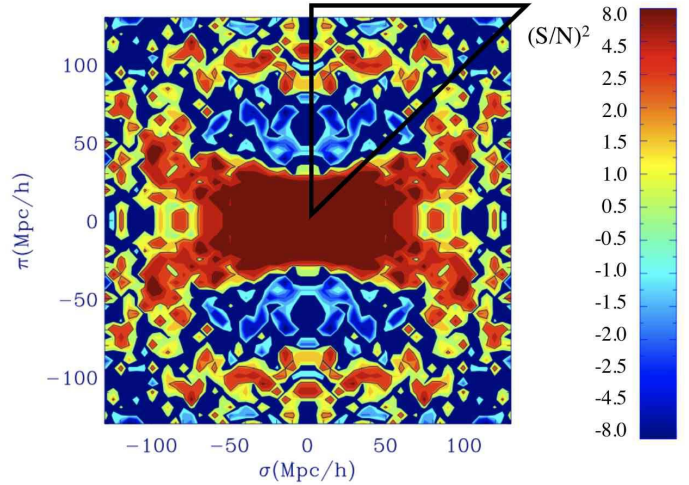


**Figure 11.** Signal-to-noise ratio in  $\xi(\sigma, \pi)$  for the  $z=0.15-0.30$  slice. The color scheme denotes  $(S/N)^2$  multiplied by the sign of the signal i.e. negative values correspond to a negative signal. The triangle highlights the region  $\pi > \sigma$ , which receives little weight in the monopole.

I), but these variations do not change the location of the BAO peak, as will be discussed below.

### 3.8 The Radial Peak

In this section, we turn our focus to the correlation function in the LOS/radial direction. A visual impression of the LOS  $\xi$  in the full sample can be gained from Fig. 12, 13 and Table 1, which will be explained in more details below. What we would like to do first is to check for systematics and test the robustness of our measurement. Then, we will examine the statistical significance of the BAO feature.

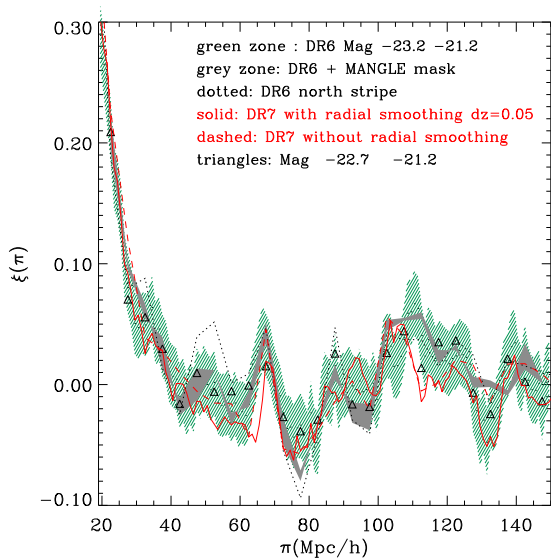


**Figure 12.** This figure shows  $\xi(\pi)$  measured using different radial selection functions, masks and datasets, for  $z = 0.15 - 0.47$ . Details are described in the text. Here, the LOS correlation is binned in  $(\sigma, \pi)$  pixels of 5 Mpc/h by 5 Mpc/h. Each pixel has  $\sigma$  extending from 0.5 Mpc/h to 5.5 Mpc/h (the minimum  $\sigma$  of 0.5 Mpc/h is imposed to avoid the fiber collision zone). The LOS correlation is plotted centered around  $\pi$  increments of 1 Mpc/h - there is therefore an overlap between pixels in the  $\pi$  direction. This is purely for presentation purpose, to show how results change for different bin center positions.

### 3.8.1 Tests for Systematics

There are many checks that need to be made, some of which we have already mentioned. Here, we provide a complete list.

1. Finite volume effects or integral constraint bias, namely an estimation bias that results from the galaxy survey having a finite size, is examined in §3.2 using large numerical simulations. We find that for the scales of interest, the integral constraint bias is totally negligible compared to errorbars.

2. We also employ numerical simulations to test the accuracy of our (statistical) error model. This is done in §3.3 (see Fig.5). We find that our error model agrees well with the Jack-knife error and also, in the case of simulated data, with the true error estimated from Monte Carlo realizations.

3. We test for robustness against a different choice of the radial selection function. In Fig. 12, the green zone shows the one sigma region of our fiducial measurement from DR6. This fiducial measurement, which is used in the rest of this paper, uses a radial selection function which is exactly the observed  $dN/dz$  from data but smoothed in bins of  $dz = 0.01$ . The red solid and dashed lines in the same figure show measurements from Data Release 7 (DR7), with different choices of the radial selection function - the solid line uses a radial selection smoothed with  $dz = 0.05$ ; the dashed line uses a radial selection that is not smoothed at all i.e. it uses  $dN/dz$  straight from the data. We can see that the resulting  $\xi(\pi)$  is, to within errors, stable against these different assumptions about the actual radial selection function.

4. We test for robustness against a different choice of the angular mask. After the release of DR6, Swanson et al. (2008) provided mask information in a readily usable form, translating the original mask files extracted from the NYU Value-Added Galaxy Catalog (Blanton et al. 2005), from MANGLE into Healpix format (Górski et al. 2005). Paper I describes how they constructed a survey "mask" for LRGs and tested the impact of the mask on clustering measurements using mock catalogs. Here, we apply the MANGLE mask with different completeness in place of our fiducial mask to DR6, and the result is shown as the gray zone in Fig. 12, which encompass the whole range of possible completeness above zero. Our measurement appears to be stable against variation in the mask.

5. We test for the stability of our measurement when we look at different subsets of the data. The triangles in Fig. 12 show  $\xi(\pi)$  measured from a set of DR6 LRGs with a different magnitude cut. The dotted line shows  $\xi(\pi)$  measured from the north stripe of DR6. Finally, the red lines show measurements from DR7, which is about  $\sim 17\%$  larger than DR6. Again, they are all consistent with each other to within errors.

In Table 1 we list our best estimates and errors for the measurement of  $\xi(\pi, \sigma)$  along the LOS for our default DR6 mask. This corresponds to the green shaded region in Fig. 12. Because errors are correlated on scales smaller than 5 Mpc/h we give the measurements and errors in the Table smoothed with a top-hat window of total width 5 Mpc/h, this makes the analysis quite insensitive to the choice of the central bin position. The resulting covariance between these 5 Mpc/h bins is negligible in practice (see Fig.6) and the different points in the figure can be treated as independent. See also Appendix 2.4 in paper I for an extensive treatment of the covariance.

### 3.8.2 Model fitting: shape constraints

We next want to check how well the data agree with the theoretical model presented in previous sections. In particular, we are interested in assessing the statistical significance of any BAO detection. This is illustrated in Fig.13. The observed correlation function (points with errorbars) is shown in radial bins of  $\Delta\pi = 5$  Mpc/h and  $0.5 < \sigma < 5.5$  Mpc/h. We fit the data with a model consisting of the following ingredients: the real space power spectrum is controlled by  $\Omega_B$  and  $\Omega_m$  with an amplitude parametrized by  $b\sigma_8$ , where  $b$  is the linear galaxy bias; redshift space distortion is described by a Kaiser model parametrized by  $\beta$  (nonlinear pairwise velocity dispersion is kept fixed at 400 km/s but its effects are important only for scales less than  $\pi < 40$  Mpc/h); the magnification bias correction is linear in  $\pi$  (Eq. [9]), parametrized by an overall normalization  $A$  (as described in §2.3). Note that we  $A = 1$  corresponds to  $s = 1.5$ . As we allowed  $A$  to varied this corresponds to degenerate changes in  $s$  or other normalization factors. The parameters  $\Omega_B$ ,  $\Omega_m$ ,  $b\sigma_8$  and  $\beta$  are constrained by the observed monopole and quadrupole of  $\xi(\sigma, \pi)$  (Paper I). We therefore impose the following  $(1 - \sigma)$  Gaussian priors:  $\Omega_B = 0.044 \pm 0.003$ ,  $\Omega_m = 0.245 \pm 0.020$ ,  $b\sigma_8 = 1.56 \pm 0.09$  and  $\beta = 0.34 \pm 0.03$

$\pi$ (Mpc/h)	$\xi(\pi, \sigma = 3)$	error
2.5	5.870	0.0253
7.5	2.219	0.0254
12.5	0.8517	0.0254
17.5	0.3851	0.0255
22.5	0.2052	0.0256
27.5	0.0883	0.0256
32.5	0.0487	0.0257
37.5	0.0308	0.0257
42.5	-0.0020	0.0258
47.5	-0.0037	0.0259
52.5	-0.0067	0.0259
57.5	-0.0183	0.0260
62.5	-0.0077	0.0261
67.5	0.0245	0.0261
72.5	-0.0228	0.0262
77.5	-0.0353	0.0263
82.5	-0.0277	0.0264
87.5	-0.0017	0.0265
92.5	-0.0014	0.0266
97.5	-0.0042	0.0267
102.5	0.0218	0.0268
107.5	0.0407	0.0268
112.5	0.0454	0.0269
117.5	0.0244	0.0270
122.5	0.0226	0.0271
127.5	-0.0049	0.0272
132.5	-0.0274	0.0273
137.5	0.0128	0.0274
142.5	0.0073	0.0275
147.5	-0.0001	0.0276

**Table 1.** Our best estimates of the 2-point correlation  $\xi(\pi, \sigma)$  in the LOS for  $0.5 < \sigma < 5.5$  (Mpc/h). In the radial direction the correlation is binned with  $\Delta\pi = 5$  Mpc/h and we take the average correlation within that bin. The covariance between bins is negligible when using this binning. This is for  $z = 0.15 - 0.47$ .

(the prior on  $\Omega_B$  is from WMAP5, while the rest is from Paper I). We hold fixed  $h = 0.72$ ,  $\sigma_8 = 0.85$  and  $n_s = 0.96$ , which are mostly degenerate with the other parameters, but verify that relaxing them in a manner consistent with current data does not alter our conclusions significantly. We allow  $A$  to vary anywhere between  $-1$  to  $5$  (flat prior). Lastly, we also allow for a shift  $D_r$  in the radial scale  $\pi$  to account for the fact that we do not know the true value of  $E(z) \equiv H(z)/H_0$  to convert the measured redshift into the radial distance  $\pi$ . Note that we can take this to be independent of  $\Omega_m$  in  $H(z)$ , even for a flat universe, as this would correspond to variations in the DE equation of state  $w$  which does not alter the shape of the correlation on linear scales. We define

$$D_r \equiv \frac{H_f(z)}{H(z)} = \frac{E_f(z)}{E(z)} = \frac{\sqrt{0.25(1+z) + 0.75}}{E(z)} \quad (13)$$

where  $E_f(z)$  corresponds to the fiducial flat LCDM cosmology with  $\Omega_m = 0.25$  used in our analysis.

The best fit model (to the full sample) is shown as a solid black curve in Fig. 13. Here, the range of scales on which the fit is performed is  $\pi = 40 - 140$  Mpc/h. The best  $\chi^2$  of the fit is  $\chi^2 \simeq 8$  for 14 degree of freedom (as la-

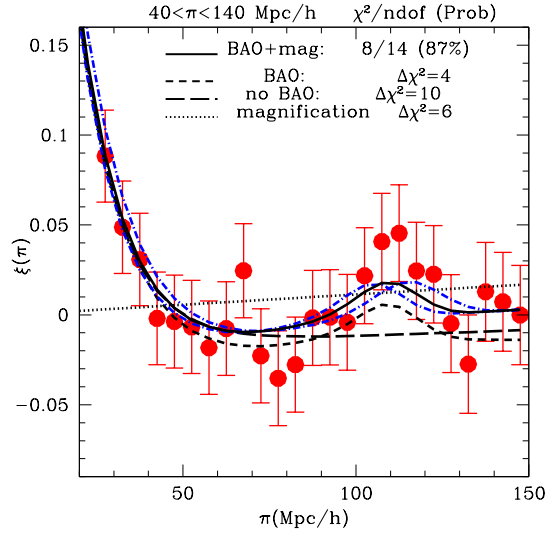


**Figure 13.** Points with 1-sigma errorbars show the measured LRG correlation  $\xi(\sigma, \pi)$  along the LOS (for  $0.5 < \sigma < 5.5$  Mpc/h) in the full SDSS sample ( $z=0.15-0.47$ ) as given in Table 1. The solid black line is the best-fit model as described in text. The dotted black (straight) line shows the contribution from magnification bias. The dashed black line with no-BAO feature is a no-wiggle model. The dashed black line with a BAO feature is a no-magnification-bias model. The  $\chi^2$  for the best-fit, and the  $\Delta\chi^2$  for the two dashed lines are given at the top of the figure. The dot-dashed blue lines show the  $1 - \sigma$  range allowed by a shift  $D_r$  in the radial scale  $\pi$ .

beled in the figure), which is reasonable (gives a probability of  $Prob = 87\%$ ). We can use this model fitting procedure to address the reality of the BAO feature: is it supported by data? A model with no BAO (generated according to Eisenstein & Hu 1998) leads to a  $\Delta\chi^2 = 10$  away from the best-fit i.e. it is ruled out at the  $3.2\sigma$  level.

It is also interesting to ask to what extent the magnification bias correction is required. We find the magnification bias normalization  $A = 4.5 \pm 2.2$ . Another way to put it is that a model with no magnification bias leads to a  $\Delta\chi^2 = 4$  away from the best-fit. The data favor a non-zero magnification bias correction at the  $2\sigma$  level. Our estimate for magnification bias,  $A = 1$ , is 1.5-sigma away from the actual best fit. Although this is not a very significant deviation, it might hint that the real lensing effect is larger than the prediction in the Appendix. This could be caused by a slope  $s > 1.5$  or by the combination of non-linear redshift space distortions and non-linear bias, which are hard to model.

We should also mention that a simple  $\xi = 0$  model carries a  $\Delta\chi^2 = 6$ , and so it is only slightly disfavored compared to the best-fit model. However, a  $\xi = 0$  model is clearly not a good description of the data once we include smaller scales.

The radial shift parameter  $D_r$  is constrained to be:

$$D_r = 0.998 \pm 0.037 \quad (1\sigma) \quad (14)$$

when we marginalize over the other parameters. The best fit value of  $D_r$  is very close to our fiducial LCDM model with  $\Omega_m = 0.25$ . The  $\pm 1$ -sigma range (i.e. models with  $D_r =$

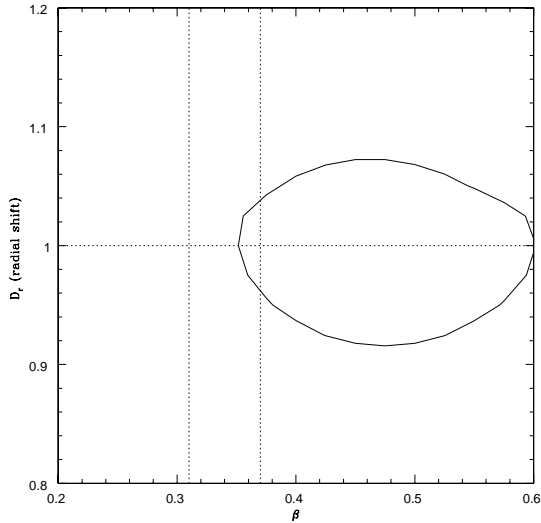


**Figure 14.** Joint constraints on the radial shift parameter  $D_r$  and  $\beta$  when no prior is assumed on  $\beta$ . The solid curve shows the  $\Delta\chi^2 = 1$  contour. The vertical lines delimit the  $1 - \sigma$  region on  $\beta$  from the observed quadrupole and monopole (Paper I).

1.035 and  $D_r = 0.961$ ) are shown in Fig.13 as blue dot-dashed lines around the best fit model (black solid line). The corresponding value of  $H(z)$  is shown in the top entry of Table 3. In principle one could find stronger constraints in  $D_r$  by fitting to smaller  $\pi$  scales, but this will be sensitive to the modeling of nonlinear redshift space distortions (i.e. finger-of-god).

Next, we investigate the robustness of our model fits. We have systematically explored the constraints on  $D_r$  when the priors are relaxed. An example is shown in Fig. 14. Here, we remove the prior on  $\beta$ . The central value for  $D_r$  remains remarkably robust. The errorbar on  $D_r$  does increase, as expected, but it is not unduly large. The best-fit  $\beta$  from the LOS data (with no prior on  $\beta$ ) lies outside the  $1 - \sigma$  region from the quadrupole and monopole data, but the errorbar from LOS data alone is quite large and there is overlap between constraints from the two different kinds of data.

We have also investigated what happens if we fit to a different range of scales  $\pi = 70 - 140$  Mpc/h. The best fit model has  $\chi^2 = 8$  for 8 degrees of freedom. A model with no BAO has a  $\Delta\chi^2 = 10$  from the best fit, and a model with no magnification bias has a  $\Delta\chi^2 = 4$  for the best fit. The results are therefore quite similar to those from  $\pi = 40 - 140$  Mpc/h, but the errors on  $D_r$  in Eq.14 increase by almost a factor of 2 for  $\pi = 70 - 140$  Mpc/h, indicating that the  $H(z)$  constraint is partially driven by the shape of the correlation rather than by just the position of the radial BAO peak. We will show in next section how to measurement the BAO peak position with independence of the shape, which will provide an absolute measurement of  $H(z)$  (independent of  $h$ ).

Fig.15 shows the same analysis for the nearby redshift slice  $z = 0.15 - 0.30$  which has lower density and much larger errorbars. The qualitative results are nevertheless similar:

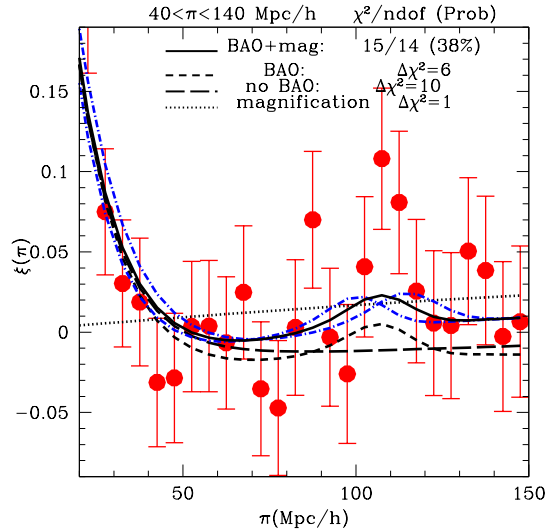


**Figure 15.** Same as Fig.13 for  $z = 0.15 - 0.30$ .

the model fits the data well, the no-BAO model is ruled out with  $\Delta\chi^2 = 10$  and the model without magnification is ruled out to  $\Delta\chi^2 = 6$ . The value of  $D_r$  is close to unity but constraints on  $D_r$  increase to about 7% as indicated by the dot-dashed lines in the figure.

For a global view of how well the model and the data agree, see Fig.10 in paper I, where we plot the data plus model in the  $\sigma - \pi$  plane for the full sample. Visually, it looks quite good. Doing a detailed overall fit to  $\xi(\sigma, \pi)$  is complicated in practice because of the small scale modeling (eg see Cabré & Gaztañaga 2009b). We leave this task for a future analysis and focus here in the line of sight data.

### 3.8.3 The BAO Feature

Next, we would like to focus on the BAO feature in the LOS around 110 Mpc/h, and assess its statistical significance without recourse to model fitting like in the last section. We compute the  $\chi^2$  against a null signal i.e.  $\chi^2 = (S/N)^2$  where  $S$  is simply the observed  $\xi$  itself. The result is plotted in Fig.16 where we show results for the full sample and for the low and high redshift slices. Dotted lines use the full covariance in Fig.6, while solid lines neglect the covariance<sup>3</sup>. The difference is small reflecting a small covariance in the radial distance. The bin width is 5 Mpc/h, so there are 2-3 independent measurements across the BAO peak. A peak is clearly detected except from the intermediate redshift slice,  $z=0.3-0.4$ , which is not plotted here ( $\chi^2$  just fluctuates inside the 2-sigma region). Errors are bigger in this  $z=0.3-0.4$  slice

<sup>3</sup> Suppose we label the pixels by  $i$ . At pixel  $i$ , the  $\chi^2$  neglecting covariance is  $\xi_i^2/C_{ii}$ , and the  $\chi^2$  including covariance is  $\sum_j \xi_i C_{ij}^{-1} \xi_j$ . Here,  $\xi_i$  is the signal at pixel  $i$ , and  $C_{ij}$  is the error covariance between pixel  $i$  and pixel  $j$ , and  $C_{ii}$  is simply the diagonal variance at pixel  $i$ .

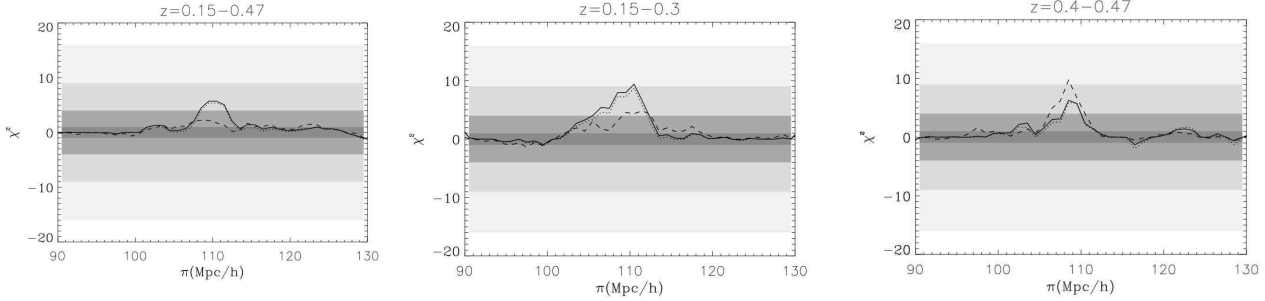


**Figure 16.** In this figure we plot the significance of the detection (away from zero) as  $\chi^2 = (S/N)^2$  without covariance (solid line) and including the covariance (dotted line) for bins of 5 Mpc/h (incrementing in steps of 1 Mpc/h). We also plot the results for a more conservative mask and a smoother selection function (dashed lines). Each panel corresponds to a different redshift slice, as labeled in the figures. The gray zones indicate a 1- $\sigma$ , 2- $\sigma$ , 3- $\sigma$  or 4- $\sigma$  detection

because there are fewer number of pairs in the radial direction at these scales. This sub-sample also has a lower galaxy bias because it includes less luminous galaxies (see Paper I), hence a lower signal and, consequently, less signal-to-noise (recall we are shot noise dominated).

To assess the effects of possible systematics, we have repeated the analysis using an angular mask with 10-20% less area (and fewer galaxies), which are safely inside “good” plates, and with a radial selection function which is smoother ( $dz=0.05$ ) than our default value of  $dz=0.02$  (see Appendix in Paper I). The results are shown as dashed lines in Fig.16. The BAO peak remains significant in both the low and high redshift slices, but less so for the full sample. We should emphasize, however, this last statement on the full sample only pertains specifically to the  $(S/N)^2$  right around the BAO feature at 110 Mpc/h. When we carry out a model fitting to the full sample over a wider range in scales (e.g. 40 – 140 Mpc/h), we find that a no-BAO model is in fact always disfavored by more than  $3\sigma$ , regardless of the mask or radial selection function (see §3.8.2 and Fig.13).

#### 4 A DIRECT DETERMINATION OF $H(Z)$

Our discussions above suggest we could attempt to infer  $H(z)$  from the LOS data in two ways. One is to carry out a model fitting as in §3.8.2. Constraints on the shift parameter  $D_r$  can be translated directly into constraints on  $H(z)$ . The result we find is shown as the first entry in Table 3. The statistical error comes from the marginalization explained in the above section, while the systematic error correspond to the difference in  $D_r$  when we use the different versions of the data shown in Fig.12. We call this the “Shape Method”. Note that this method gives  $H(z)$  in units of  $H_0$  and it relies on not just the BAO feature around 110 Mpc/h, but also the shape of the correlation function on smaller scales. Such a method is very analogous to how  $(D_A^2/H)^{1/3}$  is inferred from the monopole data in the discovery paper by Eisenstein & etal (2005).

Sample z range (mean)	$r_{\text{BAO}} \pm \sigma_{st} \pm \sigma_{sys}$ Mpc/h	$\Delta z_{\text{BAO}} \pm \sigma_{st} \pm \sigma_{sys}$
0.15-0.30 (0.24)	$110.3 \pm 2.9 \pm 1.8$	$0.0407 \pm 0.0011 \pm 0.0007$
0.15-0.47 (0.34)	$110.5 \pm 3.6 \pm 2.1$	$0.0428 \pm 0.0014 \pm 0.0008$
0.40-0.47 (0.43)	$108.9 \pm 3.9 \pm 2.1$	$0.0442 \pm 0.0015 \pm 0.0009$

**Table 2.** The BAO fiducial scale  $r_{\text{BAO}}$  in the LOS direction calculated with a flat reference  $H_{\text{ref}}(z)$  cosmology of  $\Omega_m = 0.25$ , for three redshift slices: in parenthesis is the respective pair-weighted mean redshift, and  $\sigma_{st}$  and  $\sigma_{sys}$  are the statistical and systematic errors on  $r_{\text{BAO}}$ . The direct  $\Delta z_{\text{BAO}}$  measurement is shown in the third column, which relates to the fiducial scale as  $\Delta z_{\text{BAO}} = r_{\text{BAO}} H_{\text{ref}}(z)/c$  and is independent of the value chosen for  $H_{\text{ref}}(z)$ .

#### 4.1 The Peak Method

The second method to measure  $H(z)$  is less model dependent and focus entirely on the BAO feature around 110 Mpc/h. We find the peak location, and use that as a standard ruler to measure the radial distance. We call this the “Peak Method”. We will compare both methods in this section. Note that in the shape method we will only constraint  $H(z)/H_0$  while in the peak method we will get  $H(z)$  directly.

Operationally, for the peak method, we use the relation:

$$H(z)_{\text{true}} = \frac{r_{\text{BAO}}}{r_{\text{WMAP}}} H(z)_{\text{ref}} \quad (15)$$

where  $r_{\text{WMAP}} = 153.3 \pm 2.0$  Mpc (Table 3 in Komatsu et al. (2008)) is the comoving acoustic scale inferred the cosmic microwave background (WMAP5), and  $r_{\text{BAO}}$  is the apparent BAO scale inferred from data using the fiducial expansion rate  $H(z)_{\text{ref}} = H_0 \sqrt{0.25(1+z)^3 + 0.75}$  to convert redshifts to distances.

#### 4.2 Statistical Error

The peak measured in the radial direction is broad, just as expected from the BAO signal (see Fig.13). We will take the BAO position to correspond to the location of the maximum in the  $(S/N)$  around the broad BAO peak, and we will use Monte Carlo simulations to estimate the associated errorbar.

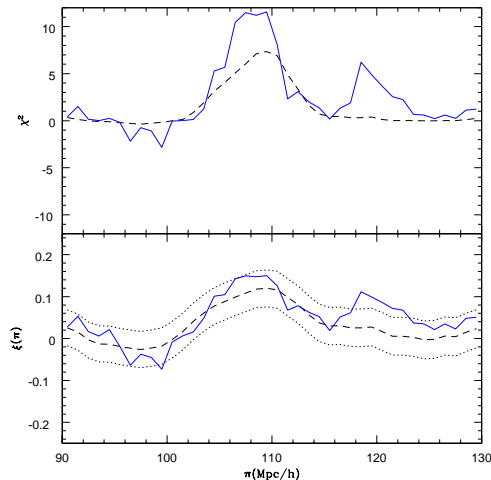


**Figure 17.** *Lower panel:* dashed line and dotted lines show the mean and dispersion for a model of the correlation function in the radial direction for the redshift slice  $z=0.15-0.30$ . This model uses a smoothed version of the real data as the baseline (the mean). The continuous line shows one of the  $10^4$  Monte Carlo realizations, which have noise added in a way that accounts properly for covariance seen in the data. *Top panel:*  $\chi^2 = (S/N)^2$  in the model (dashed line) and in the same one Monte Carlo realization (continuous line).

The resulting fiducial BAO scale location  $r_{\text{BAO}}$  are shown in Table 2.

The Monte Carlo simulations are generated as follows. We model the signal as a smoothed version of the data. We use a top-hat smoothing of 5 Mpc/h width and radial bins centered in 1Mpc/h intervals. Such a model is shown as a dashed line in Fig.17 for the sample  $z=0.15-0.30$ . Given the model, we then add noise with the same covariance and binning as in the real data. A detailed discussion of our noise model, and the tests we have applied to it, is given in §3.3. Note that while we have chosen pixels of 5 Mpc/h in size, the data actually contain information on finer resolution. In our analysis and in our simulations, the pixels are in fact incremented in the  $\pi$  direction by steps finer than 5 Mpc/h to facilitate the search for the BAO peak, and the full covariance between these overlapping (and non-overlapping) pixels is taken into account.

Fig.17 shows one realization of such simulations. For each realization, we infer the BAO peak location using exactly the same method as applied to real data. We repeat this  $10^4$  times and estimate the distribution of the inferred BAO peak location. The errorbar is given by the difference between the inferred peak location and the input BAO scale in the model. The distribution of fractional error in the BAO location, and the distribution of peak  $\chi^2 = (S/N)^2$  values, are shown in Fig.18 for the same  $z = 0.15 - 0.30$  sample. We find an rms fractional error between 2.6 and 3.5%, depending on the redshift sample used. The resulting errorbars in the peak location are shown as  $\sigma_{st}$ , the statistical error, in Table 2.

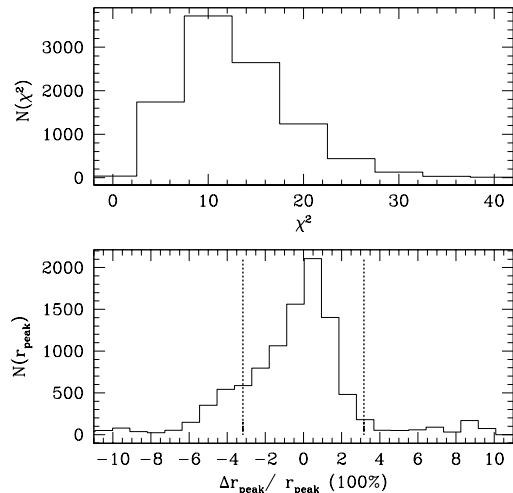


**Figure 18.** *Lower panel:* Distribution of relative values in the BAO peak location in  $10^4$  Monte Carlo simulations, taking a smoothed version of the data as the mean for the redshift slice  $z=0.15-0.30$ . *Top panel:* Distribution of peak values of  $\chi^2$ . Here,  $\chi^2 = (S/N)^2$  with  $S$  being the difference between  $\xi$  and zero i.e. this is  $\chi^2$  against null detection.

### 4.3 Systematic Error

There are two sources of systematic errors. One arises from the measurement process, and the other is theoretical in nature. Let's discuss the theoretical one first. Recently, Sanchez et al. (2008) undertook a thorough investigation of systematic effects in the determination of the sound horizon from the galaxy correlation function. Their Fig. 2 shows that at  $\Omega_m = 0.25$ , the peak in the correlation function systematically underestimates the true sound horizon by about 1.5% (this error increases to 2% for  $\Omega_m = 0.2$  and reduces to 1% for  $\Omega_m = 0.3$ ). One can understand this result by modeling the monopole correlation as a sum of a power-law and an Gaussian peak center on the BAO position. As we change the power-law index and the relative amplitude of the peak the maximum of the correlation can shift with respect to the maximum of the Gaussian. This effect should be different (and weaker) for the LOS, because the underlying correlation is flatter (and in fact slightly increasing with scale). On the other hand, magnification bias tends to move the peak by a similar amount in the opposite direction (Hui et al. 2007). Correcting for these biases is in principle possible, but requires accurate LOS modeling which is not currently feasible.

A larger source of systematic uncertainty comes from the model used in the Monte Carlo simulations in the previous section. If instead of the data or a smoothed version of the data, we take our best fit theoretical model in section 3.8.2 as the mean input to the Monte Carlo noise realizations we find a much larger error in the BAO position, of size 4 – 8% depending on the different assumptions. The reason for this is that the model has a lower amplitude than the data around the peak and models are quite degenerate to uncertainties in the cosmological parameters. Even when

Shape Method		
redshift range	$z_m$	$H(z) \pm \sigma_{st} \pm \sigma_{sys}$ km/s/Mpc $h_{72}$
0.15-0.47	0.34	$83.87 \pm 3.10 \pm 0.84$
Peak Method		
redshift range	$z_m$	$H(z) \pm \sigma_{st} \pm \sigma_{sys}$ km/s/Mpc
0.15-0.30	0.24	$79.69 \pm 2.32 \pm 1.29$
0.15-0.47	0.34	$83.80 \pm 2.96 \pm 1.59$
0.40-0.47	0.43	$86.45 \pm 3.27 \pm 1.69$

**Table 3.** The inferred  $H(z)$  with its associated errors, ie statistical and systematical, for each redshift slice. The top entry corresponds to fitting the shape of the LOS correlation to models and marginalized over cosmological parameters (note that this is in units of  $H_0 = 72h_{72}$  Km/s/Mpc). Bottom values use the Peak Method explained in Section 4.1, which is model independent.

this is not a statistically significant departure, the smaller amplitude in the model results in a large degradation in the recovered error in the peak position. We can of course choose models that have higher peak amplitude, and that are still allowed by the data. Those models will provide artificially small errorbars.

We can account for this systematic deviations in a model independent way by noticing that the observations must in fact result from the true model plus a realization of the noise. Thus, if we add noise to the observations we will in fact explore, by definition, all possible models that can agree with the data. We can use these new sets of models (data+noise realizations) as a new baseline to our Monte Carlo simulations and explore how much different the error can be when we allow for a variation in the baseline. We have run 500 such data+noise realizations and have run  $10^4$  Monte Carlo simulations for each of them (as in previous section) to find the distribution of possible errors. The result is shown in Fig. 19 for the  $z=0.15-0.30$  slice. The variance in the resulting distribution provides us with an estimate of the systematic uncertainty in our error determination.

The statistical  $\sigma_{st}$  error is taken to be the variance when we use just the data as a based model rather than the mean in the distribution of errors from data+noise, which is larger because the error has been added twice.

An additional source of our systematic error is estimated by taking the difference between results obtained using different angular masks and selection functions (see Fig. 12 and associated text). Note that our results do not change significantly when we use different masks in DR6 or even the DR7 data, which became available after the first version of this paper. This is then added to the above systematic error to produce  $\sigma_{sys}$  given in Table 2. Errors are then propagated to  $H(z)$  in Table 3.

One additional source of systematic error might have occurred to the reader. Our estimate of the BAO scale is not strictly from the LOS direction: as discussed in §3.8, we have used an array of pixels extending in the  $\pi$  direction but

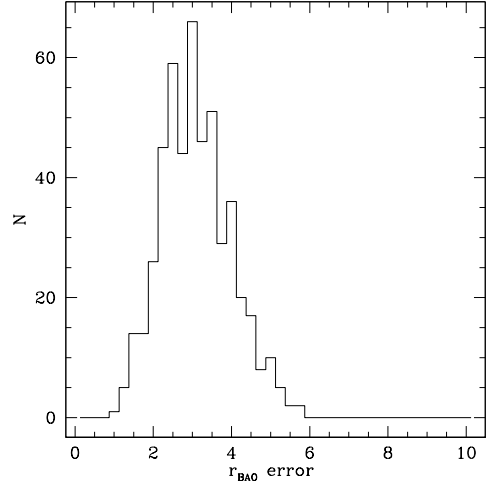


**Figure 19.** Distribution of errors in the peak positions using 500 different baseline models (each model being a realization of the data plus noise). For each baseline model we do  $10^4$  montecarlo simulations to estimate the corresponding distribution and error (ie as in lower panel of Fig.17). The variance in this distribution gives us an estimate of the error in the error. This is for the redshift slice  $z=0.15-0.30$ .

with  $\sigma = 0.5$  Mpc/h to 5.5 Mpc/h, instead of being centered at  $\sigma = 0$  (to avoid the fiber collision zone). This amounts to approximating the BAO scale  $r = \sqrt{\pi^2 + \sigma^2} \sim \pi$ . The lowest order fractional correction is  $(\sigma/\pi)^2/2 \sim 4 \times 10^{-4}$  which is negligible.

#### 4.4 Results on $H(z)$

Table 3 summarizes the different  $H(z)$  estimations and corresponding errors. The values of  $H(z)$  from the “Peak Method”, ie using Eq.(15), for the low ( $z=0.24$ ) and high ( $z=0.43$ ) redshift slices are independent of each other because they come from galaxies that are far apart. These values are the main result of this paper, as they are both model and scale independent (see previous section). In contrast, the values from the “Shape method” have been shown to depend on the range of scales used in the fit. The main virtue of this “shape method” is to show that the LOS correlation agrees well with the BAO prediction, which indicates that measured peak does in fact correspond to the BAO.

The values of  $H(z)$  from the peak method are independent of and in excellent agreement with the predictions for  $H(z)$  according to the current combined constraints from WMAP5, supernovae Ia and the monopole BAO Komatsu et al. (2008), assuming a flat LCDM cosmology (ie  $w=-1$ ). In Fig.20 we compare our estimates with  $H_0 = 70 \pm 5$  km/s/Mpc from HST van Leeuwen et al. (2007) at  $z \simeq 0.03$  and with the  $H(z)$  inferred from WMAP5 modeling with  $H_0 = 71.9 \pm 2.6$  km/s/Mpc and  $\Omega_m = 0.258 \pm 0.030$  for a flat universe LCDM ( $w=-1$ ) Komatsu et al. (2008). For a flat cosmological constant dominated model, our measure-



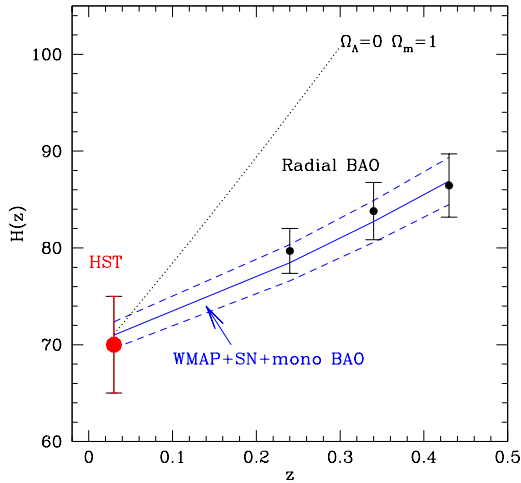


**Figure 20.**  $H(z)$  obtained using the “Peak Method” over three different redshift slices (small dots with errorbars) compared to the HST value at  $z \simeq 0.03$  (big dot with errorbar). We also plot for comparison the best value for  $H(z)$  from WMAP5 + SNIa + BAO monopole (solid line) and its associated allowed region at 2-sigma level (dashed lines), assuming a flat  $w=-1$  LCDM cosmology. For reference, the two dotted lines show the values of  $H(z)$  in open and closed models without cosmological constant.

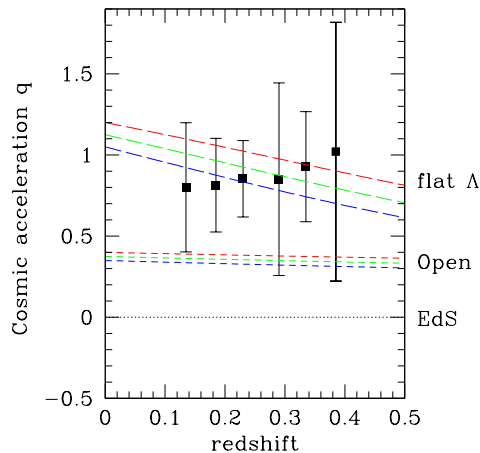


**Figure 21.** Estimates for cosmic acceleration  $q(z)$  based on the different pairs of  $H(z)$  measurements shown in Fig.20. Dashed color lines show values for flat (top lines) and open models with  $\Omega_m=0.20$  (red),  $0.25$  (green) and  $0.30$  (blue). Dotted line correspond to EdS model ( $\Omega_m = 1.0$  and  $\Omega_\Lambda = 0$ ).

ments extrapolate to

$$H_0 = 71.83 \pm 1.55 (\pm 1.03) \text{ km/s/Mpc} \quad (16)$$

if we use  $\Omega_m = 0.245 \pm 0.020$  obtained from fitting  $\xi(\sigma, \pi)$  to the same data in Paper I.

We can estimate the acceleration parameter

$$q[z] \equiv d \ln H / d \ln a + 3/2, \quad (17)$$

defined to give  $q = 0$  for the EdS (flat universe without Lambda) Cosmology. Using our two independent values of  $H(z)$  at  $z = 0.24$  and  $z = 0.43$ , we find at intermediate redshift,  $z=0.34$ :

$$q[z \simeq 0.34] = 0.93 \pm 0.33 \quad (18)$$

If instead we compare our value for the full sample  $z = 0.15 - 0.47$  at mean  $z = 0.34$  with the HST value  $H_0 = 70 \pm 5$  km/s/Mpc at  $z \simeq 0.03$  we find:

$$q[z \simeq 0.18] = 0.82 \pm 0.30 \quad (19)$$

Both results provide independent evidence for cosmic acceleration (ie away from EdS model). The mean value seems to increase with redshift which is contrary to all expectations (cosmic acceleration should turn into deceleration at high redshifts), but this trend is not significant given the errorbars. The interest of these results is that for the first time we have direct (geometrical) measurements of cosmic acceleration at different redshifts. Fig.21 shows the different estimations of  $q(z)$  for the 6 possible combinations of the 4 values of  $H(z)$ . Note that these estimates are not independent. Current errors are larger than typical evolution expected in this redshift ranged for different cosmological models (shown as dashed lines) so it is hard to conclude more with this data.

## 5 DISCUSSION & CONCLUSIONS

In this paper, we have studied in detail a peak in the LRG correlation function, in the monopole, in the circular ring on the  $\sigma - \pi$  plane, and especially in the LOS direction. Its location around 110 Mpc/h is consistent with the interpretation that it originates from baryon acoustic oscillations. Its significance can be assessed in several ways. We have performed a parametric fit to the monopole: the data requires a non-zero  $\Omega_b$  with high significance. In fact, we find that data appears to favor a value that is slightly higher than the standard WMAP5 value. However, the difference is less than  $2 - \sigma$  at both the full sample and the low redshift slice  $z = 0.15 - 0.30$ , but is larger at the high redshift slice  $z = 0.40 - 0.47$  (see Fig. 9). We have also found this tendency to high  $\Omega_b$  in paper III (Gaztañaga et al. 2008) of this series, where we analyze the BAO scale in the 3-point correlation function, which tests non-linear growth of perturbations, in contrast to the 2-point correlation function, that tests linear perturbations. Plots of the signal and the signal-to-noise of  $\xi$  in the  $\sigma - \pi$  plane (Fig. 10 and 11) provide a reassuring view of the reality of the signal: a negative valley (in blue) of negative correlations at  $\pi \sim 50 - 90$  Mpc/h together with a ring (in red) of positive correlations at  $\sim 110$  Mpc/h. The BAO peak in the LOS direction is pronounced, and detected with significance (Fig. 13 and 16).

It would be hard to explain such a peak in the 2-point monopole, in the plane  $\sigma - \pi$ , in the LOS and in the 3-point function with systematic effects. We have checked for possible systematics by varying the angular mask and the

radial selection function, and find the detection robust using either DR6 or DR7 SDSS data (see §3.8.1). The data on scales  $\pi = 40 - 140$  Mpc/h is well fit by a model that includes linear redshift space distortions, magnification bias and BAO. In fact, a model with no BAO is disfavored by the data at the  $3\sigma$  level, while a model with no magnification bias is disfavored at the  $2\sigma$  level. Our detection of the BAO modulation in the LOS direction is helped by the combination of two effects: redshift space distortions make  $\xi$  negative on scales of  $50 - 90$  Mpc/h while magnification bias gives a significant positive boost on larger scales.

We thus have significant evidence that the LOS correlation on scales  $40 < \pi < 140$  Mpc/h reproduces well the expected BAO signal. Consequently we use the LOS data to infer  $H(z)$  in two ways which we have labeled the shape and the peak method. In the shape method we have used the shape of the LOS correlation to fit  $H(z)/H_0$  marginalized over other cosmological parameters. The result is shown as the first entry to Table 3. In the peak method we find the location of the peak position and use it as a standard ruler using Eq.15. This is a more direct, geometric test in the sense that the BAO is used strictly as a standard ruler (i.e. we are not using model-dependent shape of the correlation function), and in the sense that we constrain  $H(z)$  rather than integrals thereof. The results are shown as 3 bottom entries of Table 3.

There are two parts to our error analysis. One is the errors on  $\xi(\sigma, \pi)$  itself, and the other is the errors on our measurement of the peak location. Both have been extensively tested with simulations. The error model for  $\xi$  is obtained from what is to our knowledge the largest ever cosmological simulation run to date, MICEL7680 with  $453 \text{ Gpc}^3/h^3$ ,  $2048^3$  dark matter particles and 107 million halos in a single box (Fosalba et al. 2008; Crocce et al. 2009). We are able to create out of this simulation 216 independent mock LRG catalogs, each of which has a similar size to our SDSS DR6 sample. Our mock catalogs have the same number density and very similar 2- and 3-point functions compared to data. Fig.A1 shows, for the first time on BAO scales, a comparison of the redshift space LOS linear model with non-linear measurements from simulations. Both model and simulation show very similar shapes and a prominent BAO peak which validates both our modeling and our simulated mocks. The error model constructed from these simulations is further validated by a comparison with jack-knife errors obtained from the data itself. Further details can be found in §2.3 and Fig.5.

The other part of our error analysis consists of using Monte Carlo simulations to simulate our peak measurement process. This is described in §4.2. This method involves a further systematic uncertainty: because the data is quite noisy we can not be certain of what is the true model for the mean of the Monte Carlo simulations. We have used the data itself (or a smooth version of it) to measure both the statistical and systematic errors on these measurements. Thus, these errors are more model independent than the ones in the shape method, which depend strongly on the range of scales used for the fit.

Given our measurements of  $H(z)$ , it is natural to ask:

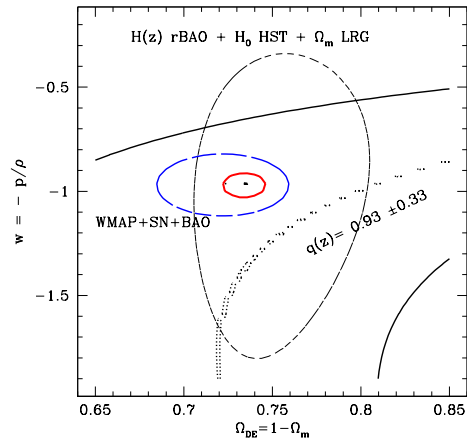


**Figure 22.** The dotted line and continuous (black) open contours across the figure show the best fit and 1-sigma contour from  $q[z = 0.34]$  in Eq.18, ie using only our two independent  $H(z)$  measurements. Long-dashed line contour show  $\Delta\chi^2 = 6.18$  (2-sigma for 2 dof) constraints from combining our  $H(z)$  measurements with  $H_0$  from HST and our  $\Omega_m$  estimate from redshifts distortions (Paper I). Short-dashed contours (blue) show the corresponding  $\Delta\chi^2 = 6.18$  constraints from the external data-set WMAP5, SNIa and BAO monopole. The inner red continuous contour shows  $\Delta\chi^2 = 1$  when combining both measurements.

what constraint do they put on the dark energy abundance and equation of state? Our measurements of  $H(z)$  at  $z = 0.24$  and  $z = 0.43$  by themselves only weakly constrain  $\Omega_{DE}$  and  $w$ . The constraint comes essentially from the acceleration parameter  $q(z)$  in Eq.18. The mean and 1-sigma constraints on  $\Omega_{DE} - w$  from  $q(z)$  are shown as dotted and continuous black open contours across Fig.22. These constraints are very weak as compared to the constraints from WMAP5 + SN + monopole BAO Komatsu et al. (2008), which are shown for  $\Delta\chi^2 = 6.18$  as a long-dashed (blue) line contour in Fig.22. The large short-dashed (black) line contour corresponds to the 2-sigma constraints when we combine our  $H(z)$  measurements with  $H_0 = 70 \pm 5$  km/s/Mpc, based on the HST analysis van Leeuwen et al. (2007), and our best fit  $\Omega_m = 0.245 \pm 0.020$  using the same LRG data in Paper I. The 2-sigma contours from the two independent data sets agree well, which is not trivial specially given the different assumptions and measurements involved in each data set. Combining both data sets, we find

$$w = -0.957 \pm 0.053 \quad (20)$$

$$\Omega_{DE} = 0.734 \pm 0.023 \quad (21)$$

which is shown as red continuous contour in Fig.22. This is in excellent agreement with the cosmological constant model. The improvement in the error with respect to the 1-sigma WMAP5+SN+BAO value of  $w = -0.97 \pm 0.06$  and is quite modest. A separate paper presents the implication on cosmological parameters when using our radial BAO scale measurements in a way that is independent of  $H_0$  (Gaztanaga et al. 2008).

To illustrate what might be achievable in the near fu-

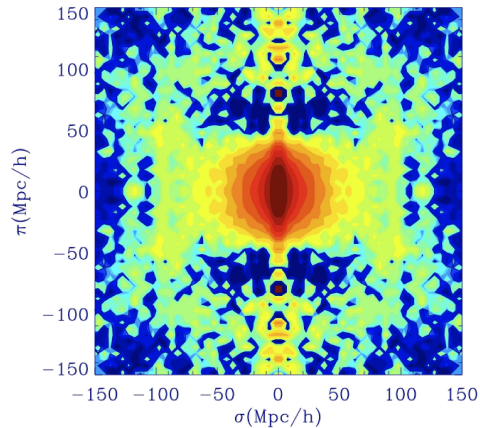


**Figure 23.**  $\xi(\pi, \sigma)$  in data for the  $z=0.15-0.30$  slice recalculated from real LRG positions with an added photo- $z$  error of  $0.003(1+z)$  as predicted for the PAU survey. It should be compared with middle panel of Fig.10 which uses spectroscopic redshifts.

ture, we show in Fig. 23 the expected  $\xi(\sigma, \pi)$  for the PAU survey (Benitez et al. 2008) which has a photo- $z$  accuracy of  $0.003(1+z)$ . We redo the analysis using current SDSS data (slice  $z=0.15-0.30$ ) but we disperse the LRG positions by this photo- $z$  error (we assume a Gaussian distribution with  $0.003(1+z)$  dispersion). The BAO signal does not appear to be washed away, as shown in Fig. 23. This is expected because the BAO peak is broader than the scale corresponding to the photo- $z$  dilution. The PAU Survey proposes to map over 10 times the SDSS DR6 volume, ie to  $z=0.9$  (this is a factor of 3 in sampling variance error) with 20 times the LRG number density (ie for  $L > L_*$ ) so shot noise will be negligible. All this should increase the signal-to-noise over SDSS DR6 by better than a factor of four. Thus, there is potential for a substantial improvement in the near future for the  $H(z)$  measurements using the techniques presented here.

## ACKNOWLEDGMENTS

We would like to thank Eiichiro Komatsu for pointing out an error in the value of  $r_{\text{WMAP}}$  that we used in the first version of this paper, Francisco Castander, Martin Crocce, Pablo Fosalba, Marc Manera and Ramon Miquel for their advise and support at different stages of this project. We acknowledge the use of simulations from the MICE consortium ([www.ice.cat/mice](http://www.ice.cat/mice)) developed at the MareNostrum supercomputer ([www.bsc.es](http://www.bsc.es)) and with support from PIC ([www.pic.es](http://www.pic.es)), the Spanish Ministerio de Ciencia y Tecnologia (MEC), project AYA2006-06341 with EC-FEDER funding, Consolider-Ingenio CSD2007-00060 and research project 2005SGR00728 from Generalitat de Catalunya. AC acknowledges support from the DURSI department of the Generalitat de Catalunya and the European Social Fund. LH acknowledges support by the DOE grant DE-FG02-92-ER40699 and the Initiatives in Science and Engineering Pro-

gram at Columbia University, and thanks Shiu-Yeun Cheng and Tai Kai Ng at the Hong Kong University of Science and Technology for hospitality.

## REFERENCES

- Adelman-McCarthy J. K., etal, 2008, *ApJS*, 175, 297  
 Alcock C., Paczynski B., 1979, *Nature*, 281, 358  
 Barriga J., Gaztañaga E., 2002, *MNRAS*, 333, 443  
 Benitez N., Gaztanaga E., Miquel R., Castander F., Moles M., Crocce M., Fernandez-Soto A., Fosalba P., Balles-teros F., Campa J., Cardiel-Sas L., Castilla J., Cristobal-Hornillos D., Delfino M., Fernandez E., Fernandez-Sopuerta C., Garcia-Bellido J., Lobo J. A., Martinez V. J., Ortiz A., Pacheco A., Paredes S., Pons-Borderia M. J., Sanchez E., Sanchez S. F., Varela J., de Vicente J. F., 2008, *ArXiv e-prints*, 807  
 Bernardeau F., Colombi S., Gaztañaga E., Scoccimarro R., 2002, *PhysRev*, 367, 1  
 Blake C., Collister A., Bridle S., Lahav O., 2007, *MNRAS*, 374, 1527  
 Blake C., Glazebrook K., 2003, *ApJ*, 594, 665  
 Blanton M. R., Schlegel D. J., Strauss M. A., Brinkmann J., Finkbeiner D., Fukugita M., Gunn J. E., Hogg D. W., Ivezić Ž., Knapp G. R., Lupton R. H., Munn J. A., Schneider D. P., Tegmark M., Zehavi I., 2005, *AJ*, 129, 2562  
 Broadhurst T. J., Taylor A. N., Peacock J. A., 1995, *ApJ*, 438, 49  
 Cabré A., Gaztañaga E., 2009a, *MNRAS*, 393, 1183  
 —, 2009b, *MNRAS*, 396, 1119  
 Cannon R., etal, 2007, *VizieR Online Data Catalog*, 837, 20425  
 Crocce M., Fosalba P., Castander F. J., Gaztanaga E., 2009, *ArXiv e-prints*  
 Crocce M., Scoccimarro R., 2008, *PRD*, 77, 023533  
 da Ángela J., Shanks T., Croom S. M., Weibacher P., Brunner R. J., Couch W. J., Miller L., Myers A. D., Nichol R. C., Pimblet K. A., de Propriis R., Richards G. T., Ross N. P., Schneider D. P., Wake D., 2008, *MNRAS*, 383, 565  
 Eisenstein D. J., etal, 2005, *ApJ*, 633, 560  
 Eisenstein D. J., Hu W., 1998, *ApJ*, 496, 605  
 Eisenstein D. J., Zehavi I., Nichol R., Hogg D. W., Blanton M. R., Seo H., Zheng Z., Tegmark M., 2004, in *Bulletin of the American Astronomical Society*, Vol. 36, *Bulletin of the American Astronomical Society*, p. 1460  
 Fosalba P., Gaztañaga E., Castander F. J., Manera M., 2008, *MNRAS*, 391, 435  
 Fugmann W., 1988, *A&A*, 204, 73  
 Gaztañaga E., Cabré A., Castander F., Crocce M., Fosalba P., 2008, *MNRAS* in press, 2448  
 Gaztanaga E., Miquel R., Sanchez E., 2008, *ArXiv e-prints*, 808  
 Górski K. M., Hivon E., Banday A. J., Wandelt B. D., Hansen F. K., Reinecke M., Bartelmann M., 2005, *ApJ*, 622, 759  
 Hamilton A. J. S., 1992, *ApJ*, 385, L5  
 Hogg D. W., Eisenstein D. J., Blanton M. R., Bahcall N. A., Brinkmann J., Gunn J. E., Schneider D. P., 2005, *ApJ*, 624, 54

Hui L., Gaztañaga E., 1999, ApJ, 519, 622  
Hui L., Gaztañaga E., Loverde M., 2007, PRD, 76, 103502  
—, 2008, PRD, 77, 063526  
Hui L., Kofman L., Shandarin S. F., 2000, ApJ, 537, 12  
Hütsi G., 2006a, A&A, 449, 891  
—, 2006b, A&A, 459, 375  
Jain B., Scranton R., Sheth R. K., 2003, MNRAS, 345, 62  
Kaiser N., 1987, MNRAS, 227, 1  
Komatsu E., Dunkley J., Nolta M. R., Bennett C. L., Gold B., Hinshaw G., Jarosik N., Larson D., Limon M., Page L., Spergel D. N., Halpern M., Hill R. S., Kogut A., Meyer S. S., Tucker G. S., Weiland J. L., Wollack E., Wright E. L., 2008, ArXiv e-prints, 803  
Landy S. D., Szalay A. S., 1993, ApJ, 412, 64  
Matsubara T., 2000a, ApJ, 535, 1  
—, 2000b, ApJ, 537, L77  
Moessner R., Jain B., Villumsen J. V., 1998, MNRAS, 294, 291  
Narayan R., 1989, ApJ, 339, L53  
Okumura T., Matsubara T., Eisenstein D. J., Kayo I., Hikeage C., Szalay A. S., Schneider D. P., 2008, ApJ, 676, 889  
Padmanabhan N., Schlegel D. J., Seljak U., Makarov A., Bahcall N. A., Blanton M. R., Brinkmann J., Eisenstein D. J., Finkbeiner D. P., Gunn J. E., Hogg D. W., Ivezić Ž., Knapp G. R., Loveday J., Lupton R. H., Nichol R. C., Schneider D. P., Strauss M. A., Tegmark M., York D. G., 2007, MNRAS, 378, 852  
Peebles P. J. E., 1980, The large-scale structure of the universe. Research supported by the National Science Foundation. Princeton, N.J., Princeton University Press, 1980. 435 p.  
Percival W. J., Cole S., Eisenstein D. J., Nichol R. C., Peacock J. A., Pope A. C., Szalay A. S., 2007, MNRAS, 381, 1053  
Ross N. P., da Ângela J., Shanks T., Wake D. A., Cannon R. D., Edge A. C., Nichol R. C., Outram P. J., Colless M., Couch W. J., Croom S. M., de Propris R., Drinkwater M. J., Eisenstein D. J., Loveday J., Pimblett K. A., Roseboom I. G., Schneider D. P., Sharp R. G., Weilbacher P. M., 2007, MNRAS, 381, 573  
Sanchez A. G., Baugh C. M., Angulo R., 2008, ArXiv e-prints, 804  
Sánchez A. G., Baugh C. M., Percival W. J., Peacock J. A., Padilla N. D., Cole S., Frenk C. S., Norberg P., 2006, MNRAS, 366, 189  
Sanchez A. G., Crocce M., Cabre A., Baugh C. M., Gaztanaga E., 2009, ArXiv e-prints  
Schlegel D. J., Finkbeiner D. P., Davis M., 1998, ApJ, 500, 525  
Schneider P., 1989, A&A, 221, 221  
Scoccimarro R., 2004, PRD, 70, 083007  
Seo H.-J., Eisenstein D. J., 2005, ApJ, 633, 575  
Smith R. E., Scoccimarro R., Sheth R. K., 2007, PRD, 75, 063512  
Swanson M. E. C., Tegmark M., Blanton M., Zehavi I., 2008, MNRAS, 385, 1635  
Szapudi I., 2004, ApJ, 614, 51  
Turner E. L., Ostriker J. P., Gott III J. R., 1984, ApJ, 284, 1

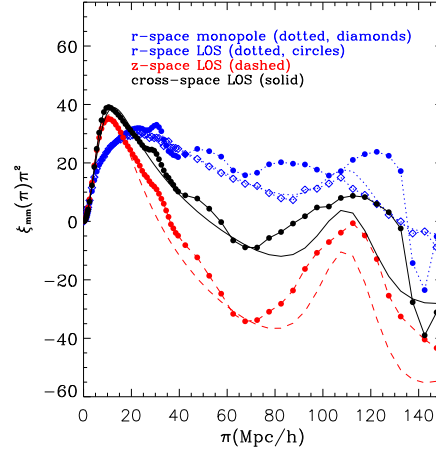


**Figure A1.** Line-of-sight (LOS) correlation averaged for  $0 < \sigma < 5$  Mpc/h. Filled circles connected by lines represent the following quantities measured from dark matter simulations: LOS mass autocorrelation in real space (blue dotted), redshift space (red dashed), cross real-redshift space (black solid). The dotted, dashed and solid lines (with no dots or circles) correspond to our analytic predictions for the LOS mass autocorrelation in real, redshift and cross space. Finally, also shown is the monopole mass autocorrelation in real space (unfilled diamonds) which agrees very well with the prediction and, modulus sampling variance, should also agree with the LOS mass autocorrelation.

van Leeuwen F., Feast M. W., Whitelock P. A., Laney C. D., 2007, MNRAS, 379, 723  
Wake D. A., Sheth R. K., Nichol R. C., Baugh C. M., Bland-Hawthorn J., Cannon R., Colless M., Couch W. J., Croom S. M., De Propris R., Drinkwater M. J., Edge A. C., Loveday J., Lam T. Y., Pimblett K. A., Roseboom I. G., Ross N. P., Schneider D. P., Shanks T., Sharp R. G., 2008, ArXiv e-prints, 802  
Webster R. L., Hewett P. C., Harding M. E., Wegner G. A., 1988, Nature, 336, 358

## APPENDIX A: NUMERICAL INVESTIGATIONS OF NONLINEAR EFFECTS

In this Appendix, we describe a number of measurements we have made to gauge the size of various nonlinear effects on the magnification bias correction to the galaxy correlation. The measurements are done on numerical N-body simulations described in the main text. Recall that the magnification bias correction to galaxy overdensity at radial distance  $\chi_2$  is given by line of sight integral:

$$\delta_\mu(\chi_2) = K \int_0^{\chi_2} d\chi \frac{(\chi_2 - \chi)\chi}{a(\chi)\chi_2} \delta(\chi) \quad (\text{A1})$$

where  $K = (5s - 2)\frac{3}{2}H_0^2\Omega_m$ . Consider now a regrouping of the terms in Eq.(7):  $\delta_{obs} = \delta_g + \delta_\mu$ , where  $\delta_g$  corresponds now to the galaxy overdensity in redshift space (i.e. including non-linear redshift space distortions). The cross-term contribution to the observed correlation function is then

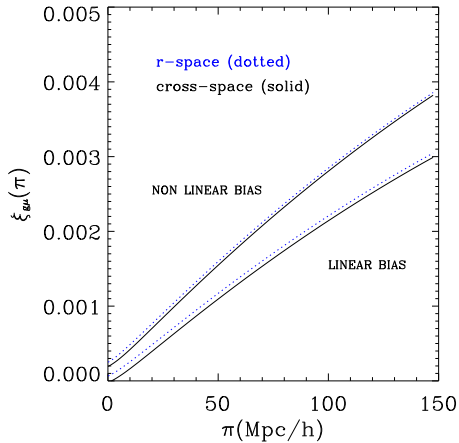


**Figure A2.** Magnification bias correction based on Eq. (A2) (which replaces Eq. [9]) for a mean redshift  $z = 0.34$ ,  $\Omega_m = 0.25$  and  $s = 1.5$  for linear (bottom lines) or non-linear (upper lines) bias using: a) the prediction of the cross-correlation  $\xi_{gm}$  in real space (dotted), b) the prediction of the cross-correlation  $\xi_{gm}$  in cross space (solid). Here, cross space means the galaxy is in redshift space and the mass is in real space. This  $\xi_{g\mu}$  is computed with the transverse separation  $\sigma$  averaged over  $0 - 5$  Mpc/h.

$\xi_{g\mu} \equiv \langle \delta_g(1)\delta_\mu(2) \rangle$ , where 1 and 2 denotes the positions of the the foreground and background galaxies. The LOS separation in redshift space is  $\pi$ , and the transverse separation is  $\sigma$ . The relevant galaxy-magnification correlation is (replacing Eq. [9]):

$$\xi_{g\mu}^{\chi_2}(\pi, \sigma) = K \int_0^{\chi_2} d\chi \frac{(\chi_2 - \chi)\chi}{a(\chi)\chi_2} \xi_{gm}(\chi_1 - \chi, \sigma) \quad (\text{A2})$$

where  $\xi_{gm} \equiv \langle \delta_g(1)\delta_m(\chi) \rangle$  is the cross correlation of galaxy fluctuations in redshift space with dark matter fluctuations in real space. Here,  $\chi_1$  is the redshift space radial distance to galaxy 1, but  $\chi_2$  and  $\chi$  are real space distances. Note that  $\xi_{gm}$  depends only on the pair separation i.e.  $(\chi_1 - \chi, \sigma)$ , while  $\xi_{g\mu}$  depends both on  $\chi_2$  and on the pair separation  $(\pi, \sigma)$ .

In our new calculation here we will fix  $\chi_2$  to be at the mean redshift of the survey, but we have also studied how the result changes when we take into account the fact that  $\chi_2$  varies across the survey (see below) - basically, if  $\chi_1$  are  $\chi_2$  are well separated,  $\xi_{g\mu}$  is almost independent of  $\chi_2$  (except indirectly through the LOS separation  $\pi$ ). One can see how Eq. (9) comes about from Eq. (A2) - take the limit in which  $\chi_2 - \chi_1 \ll \chi_2, \chi_1$ , and ignore the subtle difference between redshift space and real space distances. Our task here is to evaluate Eq. (A2) exactly using simulations.

First, as a warm-up, we use the dark matter (as opposed to halo) simulations which have the correct velocities on small scales. We compare the mass-mass correlation  $\xi_{mm}(\pi, \sigma)$  in real space, redshift space and the cross-correlation between real and redshift space. (Note:  $\xi_{mm}$  can be thought of as a first proxy to  $\xi_{gm}$ ; we will examine  $\xi_{\text{halo}, m}$  below as a better proxy.) We smooth  $\xi_{mm}(\pi, \sigma)$  in bins of 5Mpc/h, as we do with real LRG galaxies. In Fig.A1 we show

a set of N-body measurements (shown as dots connected by lines) for the dark matter LOS auto-correlation in real space (dotted blue line), redshift space (dashed red line) and in the cross-correlation of real and redshift space (solid black line). Note how the BAO peak in redshift or cross-space is enhanced quite a bit compared to that in real space. We compare these simulation results with analytic predictions (lines without dots; blue dotted for real space, red dashed for redshift space and black solid for cross-space) which combine linear theory on large scales with velocity dispersion on small scales (see paper I for an extensive explanation of the model). Note how the analytic model roughly matches the simulation data. However, despite the similarities in the shape, the amplitude of the LOS baryon peak seems slightly larger in the simulations than in the analytic model. It is not entirely clear to us how significant the difference is, but it should be noted that non-linear redshift space distortions have yet to be properly explored and modeled in the LOS direction Scoccimarro (2004). We will see a similar tendency in the actual LRG galaxies but the measurement errors are large. Ultimately, what we need is something like a LOS integral of  $\xi_{mm}$  (see Eq. [A2]). We find that the difference between integrating  $\xi_{mm}(\pi, \sigma)$  in real space, redshift space or in the cross space is not very significant.

Next, we repeat the same exercise for  $\xi_{gm}$ , using halos in the simulations as a proxy for LRGs. The conclusions are quite similar to those for  $\xi_{mm}$ . In particular, we find that as far as the LOS integral of  $\xi_{gm}$  is concerned (Eq. [A2]), it actually does not matter much whether we use  $\xi_{gm}$  in real space, redshift space or cross-space. What distinguishes  $\xi_{gm}$  from  $\xi_{mm}$  is the galaxy bias which is about 2 on large scales but rise to about 3 - 4 on small scales. As emphasized in §2.3, the nonlinear galaxy bias affects  $\xi_{g\mu}(\pi, \sigma)$  for a small  $\sigma$ , even if  $\pi$  is large. This is illustrated in Fig. A2. The correct  $\xi_{g\mu}$  using a nonlinear galaxy bias is larger than the one using a linear galaxy bias by about a factor of 1.5. Note also how the  $\pi$  dependence is close to linear, supporting the approximations made in Eq. (9).

Finally, we have also studied the effect of the chosen value for  $\chi_2$  in the integral of Eq.A2. The real magnification should be a weighting of integrals at the different redshifts (or  $\chi_2$ ) of the survey. Each redshift bin is weighted depending on the number of galaxies and the volume under this  $\chi_2$ . The exact result is almost identical to taking  $\chi_2$  to be at the median redshift of the survey.